Bridge-like lipid transfer protein 3A (BLTP3A) is associated with membranes of the late endocytic pathway and is an effector of CASM

Michael G. Hanna[1-5], Hely O. Rodriguez Cruz[1-5], Kenshiro Fujise[1-5], Zhuonging Li[6], Mara Monetti[6], Pietro De Camilli[1-5]

[1]Department of Neuroscience, Yale University School of Medicine, New Haven, CT;

[2]Department of Cell Biology, Yale University School of Medicine, New Haven, CT;

[3]Howard Hughes Medical Institute, Yale University School of Medicine, New Haven, CT;

[4]Program in Cellular Neuroscience, Neurodegeneration and Repair, Yale University School of Medicine, New Haven, CT;

[5]Aligning Science Across Parkinson's (ASAP) Collaborative Research Network, Chevy Chase, MD;

[6]Proteomics Core Facility, Sloan Kettering Institute, Memorial Sloan Kettering Cancer Center, New York, NY.

Correspondence to Pietro De Camilli: pietro.decamilli@yale.edu

Keywords

Bridge-like lipid transfer protein, BLTP, BLTP3A, BLTP3B, Rab7, lysosome, lysosomal membrane damage, CASM, mATG8, LLOMe, LRRK1, LRRK2, Rab45

ABSTRACT

Recent studies have identified a family of rod-shaped proteins which includes VPS13 and ATG2 and are thought to mediate unidirectional lipid transport at intracellular membrane contacts by a bridge-like mechanism. Here, we show that one such protein, BLTP3A/UHRF1BP1, associates with VAMP7-positive vesicles via its C-terminal region and anchors them to lysosomes via the binding of its chorein domain containing N-terminal region to Rab7. Upon damage of lysosomal membranes and resulting mATG8 recruitment to their surface by CASM, BLTP3A first dissociates from lysosomes but then reassociates with them via an interaction of its LIR motif with mATG8. Such interaction is mutually exclusive to the binding of BLTP3A to vesicles and leaves its N-terminal chorein domain, i.e. the proposed entry site of lipids into this family of proteins, available for binding to another membrane, possibly the ER. Our findings reveal that BLTP3A is an effector CASM, potentially as part of a mechanism to help repair or minimize lysosome damage by delivering lipids.

INTRODUCTION

The presence in eukaryotic cells of a multiplicity of anatomically discontinuous lipid-based intracellular membranes requires mechanisms to transport lipids between them. This is achieved both by membrane traffic (Palade, 1975) and by lipid transport proteins (LTPs) (DeGrella and Simoni, 1982; Wirtz, 1991; Reinisch and Prinz, 2021) or protein complexes that have the property to extract lipid from membranes, shield them in hydrophobic cavities and insert them into acceptor membranes. Typically, LTPs function at sites where two membranes are closely apposed, i.e. where transport may occur with greater speed and specificity (Saheki and Camilli, 2017; Wong et al., 2019; Prinz et al., 2020; Voeltz et al., 2024). Moreover, in most cases studied so far transport occurs via a shuttle mechanism in which a lipid harboring module that contains one or few lipids, is connected via flexible linkers to protein domains that tether the two membranes together. In recent years, however, the occurrence of an additional mode of lipid transport, mediated by rod-like proteins that harbor a hydrophobic groove or tunnel along which lipids can slide and which directly bridge two membranes has been described (Kumar et al., 2018; Osawa et al., 2019; Maeda et al., 2019; Valverde et al., 2019; Wong et al., 2019; Levine, 2019; Li et al., 2020; Leonzino et al., 2021; Dziurdzik and Conibear, 2021; Cai et al., 2022; Hanna et al., 2022). These proteins, collectively referred to as bridge-like lipid transfer proteins (BLTPs), are evolutionary related and have a similar basic molecular architecture (Neuman et al., 2022). Their core is represented by concatamers of small beta-sheets with a taco-like fold, referred to as repeating beta-groove (RBG) modules, which are lined by hydrophobic amino acids (a.a.) at their inner surface, thus generating a continuous hydrophobic surface (Kumar et al., 2018; Li et al., 2020; Levine, 2022; Neuman et al., 2022; Hanna et al., 2023; Kang et al., 2024; Wang et al., 2024b). Moreover, they comprise motifs or domains that allow them to tether two different membranes and a variety of loops or outpocketings of variable length which may have regulatory or protein-protein interaction functions (Dziurdzik and Conibear, 2021; Neuman et al., 2022; Adlakha et al., 2022; Hanna et al., 2023). They are thought to mediate bulk lipid (generally phospholipid) transport between membranes. As the groove at its narrowest point can only accommodate one phospholipid, such transport is thought to be unidirectional (Li et al., 2020; Kang et al., 2024; Wang et al., 2024b). BLTPs comprise VPS13, the founding member of the family, as well as the autophagy factor ATG2, and other proteins originally referred to by multiple different names in different organisms and are now renamed BLTP1, BLTP2 and BLTP3 (Neuman et al., 2022; Hanna et al., 2023). These proteins differ in the number of RBG modules and thus in length: 17 in BLTP1, the longer member of the family and six in BLTP3, the shorter family member (Levine, 2022).

The putative role of BLTPs in bulk lipid transport is ideally suited for membrane bilayer expansion or repair via the delivery of newly synthesized lipids from the ER, a possibility strongly supported by the well-established roles of yeast VPS13 in the growth of the sporulation membrane (Park and Neiman, 2012) and of ATG2 in the expansion of the isolation membrane (Wang et al., 2001; Velikkakath et al., 2012; Gómez-Sánchez et al., 2018; Osawa et al., 2019; Valverde et al., 2019). Other processes in which BLTPs anchored to the ER have been implicated also involve membrane expansion, such as biogenesis of mitochondria and of peroxisomes (Park et al., 2016; John Peter et al., 2017; Anding et al., 2018; Baldwin et al., 2021; Guillén-Samander et al., 2021),

organelles not connected to the ER by membrane traffic. In other cases, the relation of the putative bulk lipid transfer function of BLTPs to bilayer expansion is less clear, and BLTPs seem to be primarily important to control the composition of the receiving bilayer (Tokai et al., 2000; John Peter et al., 2022; Wang et al., 2022; Hanna et al., 2022). In this case delivery of new lipids to a membrane may be removed by a compensatory mechanism, for example by membrane traffic, thereby limiting expansion overall. As BLTPs have been identified only recently, much remains to be discovered about their function.

Two very similar BLTPs of which little is known are BLTP3A (also called UHRF1BP1) and BLTP3B (also called SHIP164 or UHRF1BP1L for UHRF1BP1-Like) (Hanna et al., 2022; Neuman et al., 2022). BLTP3A was originally identified as a Binding Protein (BP) of the epigenetic regulator UHRF1 (Unoki et al., 2004) and its paralogue BLTP3B was independently identified as an interactor of syntaxin 6 (Syntaxin 6 Habc-interacting protein of 164 kDa, hence its alias SHIP164) and found to localize on membrane of the endocytic pathway harboring this protein (Otto et al., 2010). BLTP3A and BLTP3B were also top hits in a screen for effectors of Rab5 and Rab7, respectively (Gillingham et al., 2019).

Following up on these earlier studies we have recently reported a systematic characterization of the properties of BLTP3B (Hanna et al., 2022). We showed that endogenous BLTP3B is localized on clusters of endocytic vesicles that interact with components of the retrograde microtubule-based transport system [dynein light chain (DYNLL1/2) (Carter et al., 2016) and Rab45 (CRACR2a) (Wang et al., 2019)] and that loss of BLTP3B results in a perturbation of the retrograde traffic to the Golgi area of the cation independent mannose-6-phosphate receptor (MPR) (Lin et al., 2003). Exogenous expression of BLTP3B, leading to its overexpression, resulted in a striking accumulation of these vesicles that formed tightly packed clusters anchored to Rab5-positive early endosomes (Hanna et al., 2022). How the putative lipid transport function of BLTP3B relate to this localization and phenotypes remains an open question.

The goal of the present study was to acquire new information about BLTP3A. We report here that BLTP3A, like BLTP3B, is localized on clusters of small vesicles anchored to LAMP1-positive organelles via Rab7 vesicles and that BLTP3A overexpression induces a massive expansion of such clusters. We further show that lysosome damage triggers the rapid loss of the Rab7-dependent association of BLTP3A with LAMP1-positive organelles, followed by its CASM (Durgan and Florey, 2022)-dependent reassociation with them in an mATG8 and LIR motif-dependent way with implications for lipid transport. Collectively, these findings point to a role of this protein at the interface between late endocytic traffic and lysosomes and also raise the possibility that BLTP3A, via its lipid transport functions, may play a role in the response to lysosome damage.

RESULTS

Close structural similarity, but different interactions, of BLTP3A relative to BLTP3B

BLTP3A is very similar to BLTP3B (41% identity and 58% positives in primary sequence). Moreover, fold-prediction algorithms (Jumper et al., 2021; Yang et al., 2020) show that BLTP3A

138 shares all the key structural features of BLTP3B: a rod-like core composed by six RBG motifs
139 (Levine, 2022), a hydrophobic groove that runs along its entire length, a large disordered
140 outpocketing of the rod-like core (a.a. 885-1188) and a C-terminal helix (a.a. 1394-1440) (**Figure**
141 **1A**). Both BLTP3A and BLTP3B are reported in Biogrid (https://thebiogrid.org) to be interactors
142 of Rab45 (CRACR2a), an adaptor for dynein and retrograde microtubule traffic (Wang et al., 2019)
143 and, accordingly, over-expression of GFP-Rab45 concentrated BLTP3A-mRFP to perinuclear
144 spots (the centrosomal area) similar to our previous findings of BLTP3B (**Supplemental Figure**
145 **1A**) (Hanna et al., 2022). Despite these similarities, BLTP3A lacks the motifs responsible for
146 binding to syntaxin-6 (Stx6) and the dynein light chain (DYNLL1/2) (**Figure 1B**), which we had
147 identified in BLTP3B (Hanna et al., 2022). Moreover, BLTP3A was shown to be an effector of
148 Rab7, instead of Rab5 (Gillingham et al., 2019). A per-residue evolutionary conservation analysis
149 of BLTP3A carried out using the ConSurf server (Armon et al., 2001; Yariv et al., 2023) revealed
150 that most conserved residues belong to the RBG motif core, particularly its N-terminal portion
151 (**Figure 1A**). Short stretches of conserved residues, however, are also present in predicted
152 unfolded loops emerging from this core, including the large outpocketing. As revealed by western
153 blotting, BLTP3A, like BLTP3B, has broad expression in different mouse tissues (**Figure 1C**), with
154 higher levels occurring in brain and lung.
155
156 **BLTP3A localizes to foci concentrated near lysosomes**
157
158 In a previous preliminary analysis of BLTP3A localization (Hanna et al., 2022) we had shown that
159 exogenously expressed fluorescently tagged BLTP3A appears as fluorescent foci localized in
160 proximity of organelles positive for the lysosome marker LAMP1 and of Rab7, a Rab associated
161 with late endosome and lysosomes (these organelles will be referred to henceforth collectively as
162 "lysosomes"). As our study of BLTP3B had shown that its exogenous expression resulted in an
163 enlargement of the BLTP3B positive compartment (vesicle clusters), we wished to confirm that
164 even endogenous BLTP3A was localized in proximity of lysosomes. Available antibodies directed
165 against BLTP3A did not detect a clear specific signal by immunocytochemistry. Thus, we turned
166 to a knock-in strategy to epitope tag the endogenous protein. Since preliminary experiments
167 revealed heterogeneity in the expression levels of BLTP3A in frequently used cell lines, we chose
168 A549 cells (lung adenocarcinoma epithelial cells) for these experiments where we detected robust
169 expression of BLTP3A, consistent with high expression of BLTP3A in the lung (**Figure 1C**).
170
171 The BLTP3A locus in A549 cells was edited by inserting after residue V904 a nucleotide sequence
172 encoding a single V5 epitope flanked on either side with short GSGSG linkers (**Supplemental**
173 **Figure 1B**). This site is within a predicted disordered region and is not expected to change the
174 lipid channel core of BLTP3A **(Supplemental Figure 1C).** Edited BLTP3A was validated by
175 Western blotting of homogenates of edited cells revealing a V5-positive band (endogenous
176 BLTP3A^V5) with the same motility as BLTP3A (**Figure 1D**).
177
178 Anti-V5 immunofluorescence of edited cells showed small weakly fluorescence puncta throughout
179 the cytoplasm, which were enriched in central regions of cells (**Figure 1E**) and were not observed
180 in WT cells immunostained under the same conditions (**Figure 1E**). Importantly, many V5-positive
181 puncta were adjacent to, or partially overlapping with, the fluorescence produced by antibodies

against LAMP1 (**Figure 1E**), consistent with BLTP3A being a Rab7 effector. The fluorescence of exogenously expressed tagged BLTP3A-GFP overlapped with anti-V5 immunofluorescence of edited cells, in agreement with our previous preliminary findings (Hanna et al., 2022), although accumulations of BLTP3A-GFP fluorescence were much larger (**Figure 1E**).

Large BLTP3A foci produced by its overexpression represent clusters of vesicles anchored to lysosomes

Given the similar localization of endogenous and exogenous BLTP3A next to lysosomes, we capitalized on exogenous BLTP3A tagged with various fluorescently tagged proteins, i.e. constructs which could be analyzed by Correlative Light-Electron Microscopy (CLEM) (immunofluorescence of the V5 epitope requires fixation and permeabilization, i.e. a treatment that perturbs cell ultrastructure). We primarily used RPE-1 cells for these studies, as LAMP1-positive organelles in these cells are very large, abundant, clustered around the Golgi complex and nucleus (**Figure 1F**), and thus easy to identify by microscopy even without specific markers. Upon co-expression of LAMP1-GFP and BLTP3A-mRFP (**Figure 1G**), two sets of BLTP3A-mRFP-positive structures were observed by fluorescence microscopy: i) BLTP3A-mRFP accumulations directly adjacent to lysosomes, often bridging two closely apposed LAMP1-GFP-vacuoles and ii) larger (often very large) BLTP3A-mRFP accumulations not obviously connected to the large LAMP1-GFP-vacuoles. Analysis of these structures by CLEM in RPE-1 cells also expressing mito-BFP (to help fluorescence - EM alignment) showed that BLTP3A-mRFP foci represented tightly packed clusters of approximately 50-70 nm vesicles (**Figure 1H**). Importantly, the vesicles of such clusters directly adjacent to LAMP1-GFP vacuoles appeared to be tethered to lysosomal membranes, with an average distance of ~10-11 nm (**Figure 1I**).

This exaggerated accumulation of large clusters of small vesicles mirrors what we had observed upon overexpression of BLTP3B, indicating that a shared property of BLTP3A and BLTP3B is to bind small vesicles, induce their accumulation, cluster them, and anchor such clusters to other organelles although clusters of BLTP3B vesicles are anchored to early endosomes (consistent with BLTP3B being an effector of Rab5), while clusters of BLTP3A are anchored to late endosomes/lysosomes (consistent with BLTP3A being an effector of Rab7). As our study of BLTP3B had shown that even BLTP3B expressed at an endogenous level is localized to vesicle clusters which are much smaller than clusters observed upon BLTP3B overexpression (Hanna et al., 2022), we hypothesized that the massive accumulation of vesicles observed upon overexpression of BLTP3 isoforms reflect a property of these proteins to nucleate biomolecular condensates. Accordingly, live imaging revealed that both clusters of BLTP3A and of BLTP3B (Hanna et al., 2022) are highly dynamic. For example, they can undergo fission into smaller clusters, as expected for a compartment with liquid-like properties.

BLTP3A positive vesicles contain VAMP7, a SNARE implicated in traffic to lysosomes

The clustering of BLTP3A-positive vesicles next to lysosomes suggested that they may represent organelles destined to fuse with them. As at least some of the vesicles that fuse with late endosomes and lysosomes harbor VAMP7 in their membrane (Advani et al., 1999; Pols et al.,

2013), we explored the potential presence of this SNARE in BLTP3A-positive vesicles (**Figure 1J**). Supporting this hypothesis, anti-VAMP7 immunofluorescence revealed a striking overlap with the fluorescence of BLTP3A-mRFP both on the isolated BLTP3A clusters and on those anchored to lysosomes (**Figure 1J**). A similar overlap was observed between the BLTP3A signal and immunofluorescence for VAMP4 (**Figure 1J**), another SNARE protein implicated in endosomal traffic (Martinez-Arca et al., 2001; Mallard et al., 2002; Tran et al., 2007). In spite of the many similarities between BLTP3A and BLTP3B, no fluorescence overlap was observed between BLTP3B-mRFP fluorescence and endogenous VAMP7 or VAMP4 immunoreactivity (**Supplemental Figure 1D**), revealing major differences in the cargo of BLTP3A and BLTP3B vesicles. However, BLTP3A-mRFP accumulations also overlapped with the immunofluorescence of endogenous ATG9A, a component of autophagosome precursor vesicles, (**Figure 1J**), as previously observed for BLTP3B-mRFP (Hanna et al., 2022) (**Supplemental Figure 1D**). As both VAMP4 and VAMP7 were reported to interact with LRRK1 and LRRK2 (Wang et al., 2018; Filippini et al., 2023), we also examined whether GFP-LRRK1 or GFP-LRRK2 can colocalize with these vesicles. While GFP-LRRK1 and GFP-LRRK2 had primarily a diffuse cytosolic localization in control cells, in a fraction of BLTP3A-mRFP expressing cells they strikingly colocalized with BLTP3A-positive accumulations (**Supplemental Figure 1E-G, Supplemental Figure 2A-B**).

The association of BLTP3A with lysosomes is mediated by its N-terminal region where the Rab7 binding site is located

To confirm that Rab7 is responsible for the association of BLTP3A-positive vesicles with lysosomes (Gillingham et al., 2019), BLTP3A-mRFP was co-expressed in RPE-1 cells with either WT RAB7 (GFP-Rab7$_{WT}$) or dominant negative (DN) Rab7 (GFP-Rab7$_{T22N}$), i.e. a mutant Rab7 that sequesters its guanylnucleotide exchange factor (GEF) to prevent formation of GTP-loaded Rab7 (**Figure 2A**) (Stenmark and Olkkonen, 2001). The coexpression of WT Rab7, which localized along the entire surface of endolysosomes, but not within the vesicle clusters, did not alter the localization of BLTP3A-mRFP (**Figure 2A**). In contrast, coexpression of GFP-Rab7$_{T22N}$ abolished the association of BLTP3A-mRFP foci with lysosomes and induced the expansion of the BLTP3A foci free in the cytoplasm (**Figure 2A**), which CLEM confirmed to represent large accumulations of vesicles no longer associated with lysosomes (**Figure 2B**).

To determine the region of BLTP3A responsible for the association with Rab7, which could provide insight into the orientation of BLTP3A at the lysosome-vesicle interface, we generated chimeras of BLTP3A and BLTP3B using BLTP3B tagged with mRFP at its C terminus as a backbone (**Figure 2C**). As BLTP3B does not associate with Rab7 in spite of its close similarity to BLTP3A, we searched for a.a. sequences of BLTP3A which would confer Rab7 binding and lysosome localization to BLTP3B. A chimera (BLTP3$_{chimera-1}$) in which its first RBG module (a.a. 1-125, which includes the so-called chorein domain) was replaced by the first RBG module of BLTP3A (a.a 1-125) formed large clusters but such clusters were not associated with lysosomes (**Figure 2D**), as expected for BLTP3B. In contrast, a chimera (BLTP3$_{chimera-2}$) in which its second RBG module (a.a. 126-319) was replaced by the equivalent module of BLTP3A (a.a. 126-322) localized to LAMP1-GFP compartments similar to WT BLTP3A (**Figure 2D**), suggesting that the second RBG module of BLTP3A is sufficient for the Rab7-dependent lysosomal localization.

Moreover, a truncated construct comprising the first 2 RBG motifs of BLTP3A plus the first β-strand of the third RBG module of the same protein resulted in a fusion protein (BLTP3A$_{1-336}$-mRFP) that localized at lysosomes (**Figure 2D & 2E**), confirming the presence of the Rab7 binding site in this BLTP3A fragment. Notably, this fragment decorated homogenously the entire lysosomal surface, without forming the foci on their surface that reflect vesicle accumulations. These findings were further supported by the exogenous expression of Rab7 constructs. Expression of WT Rab7 greatly enhanced the localization of BLTP3A$_{1-336}$-mRFP around the entire lysosomal surface (**Figure 2F**), while the expression of dominant negative Rab7 (GFP-Rab7$_{T22N}$) resulted in a diffuse localization of BLTP3A$_{1-336}$-mRFP throughout the cytosol (**Figure 2F**). We conclude that a portion of BLTP3A near its N-terminus is necessary and sufficient for the localization BLTP3A at lysosomes, suggesting that the C-terminal portion of BLPT3A is likely responsible for vesicle binding and clustering (**Figure 2G**).

To confirm that the binding site for the vesicle is contained in the C-terminal region of BLTP3A, we generated BLTP3A constructs with C-terminal deletions and expressed them in cells also expressing dominant negative Rab7 (GFP-Rab7$_{T22N}$) to determine whether they could still cluster vesicles (**Figure 3A**). Deletion of the C-terminal helix of BLTP3A and of the linker that connects this helix to the last RBG motif (BLTP3A$_{1-1364}$-mRFP) did not affect the property of BLTP3A to cluster VAMP7-vesicles (detected by immunofluorescence using antibodies against VAMP7) similar to wild-type BLTP3A. However, a further truncation (construct BLTP3A$_{1-1327}$-mRFP) including the last two beta-strands of the sixth and final RBG motif of the channel, resulted in a protein that was diffusely cytosolic and did not cluster vesicles. The only accumulation of BLTP3A observed in these cells was a single cluster close to the nucleus (**Figure 3A**), most likely reflecting its interaction with Rab45 at the centrosomal area (**Supplemental Figure 1A**), but this cluster was VAMP7 negative, in agreement with the loss of vesicle binding (**Figure 3A**) Neither C-terminal truncation abolished localization to lysosomes (**Supplemental Figure 2C**). We conclude that the C-terminal portion of BLTP3A is necessary to interface with small vesicles.

To identify BLTP3A binding partners on the vesicles, we carried out anti-V5 affinity purification from non-ionic detergent solubilized A549 cells where BLTP3A was tagged at the endogenous locus, i.e. experimental conditions optimally suited to reveal physiological binding partners (**Figure 3B**). Affinity-purified proteins were then identified by mass spectrometry (**Figure 3C**). Unedited A549 cells were used as controls. While two of the top specific hits, Rab27B and its effector melanophilin (MLPH) are membrane associated proteins of transport vesicles (Nagata et al., 1990; Ménasché et al., 2000; Hume et al., 2001; Bahadoran et al., 2001; Nagashima et al., 2002; Strom et al., 2002), we failed to obtain evidence for a concentration of these proteins on BLTP3A-positve vesicles. Thus, the relevance of these two interactions was not further investigated in this study. Two other hits were mATG8 family members (GABARAP and MAP1LC3B) which will be discussed below.

Lysosomal damage disrupts the Rab7-dependent association of BLTP3A positive vesicles with lysosomes

Perturbation of the membranes of lysosomes, for example by L-Leucyl-L-Leucine methyl ester (LLOMe), a dipeptide taken-up into lysosomes where it is metabolized into membranolytic peptides (Goldman and Kaplan, 1973; Thiele and Lipsky, 1990; Uchimoto et al., 1999), was reported to trigger the rapid recruitment of factors to their surface that may help prevent or repair damage (Skowyra et al., 2018; Radulovic et al., 2018; Shukla et al., 2022; Herbst et al., 2020; Radulovic et al., 2022; Tan and Finkel, 2022; Bentley-DeSousa and Ferguson, 2023; Wang et al., 2024a). These include ORP family members (shuttle-like lipid transport proteins) (Tan and Finkel, 2022; Radulovic et al., 2022) as well as VPS13C (Wang et al., 2024a) and ATG2 (Tan and Finkel, 2022; Cross et al., 2023), bridge-like lipid transfer proteins structurally related to BLTP3A that are thought to mediate bulk phospholipid delivery from the ER to damaged lysosomes. Although a pool of BLTP3A is already at contacts with lysosomes under control condition (the pool linking small vesicles to the lysosomal surface), we explored whether LLOMe dependent damage of lysosomes had an impact on BLTP3A in RPE-1 cells. Surprisingly, and in contrast to what was reported for VPS13C and ATG2, the focal accumulations of BLTP3A, which reflect accumulations of BLTP3A-positive vesicles, dissociated within minutes from the lysosomal surface upon lysosome damage (**Figure 4A**), whose occurrence was confirmed by the recruitment of cytosolic IST1 (mApple-IST1) (**Figure 4A**), an ESCRT-III subunit (Skowyra et al., 2018; Corkery et al., 2024). This dissociation, however, was not accompanied by a dispersion of the vesicles after LLOMe, indicating that the Rab7-dependent interaction of BLTP3A with lysosomes, not the interactions which bind and clusters vesicles, was perturbed. In fact, even the Rab7 binding N-terminal fragment of BLTP3A ($BLTP3A_{1-336}$-mRFP) dissociated from lysosomes, visualized in this experiment by the lysosomal protein NPC1 (NPC1-GFP) (**Figure 4B**). Mechanisms responsible for the dissociation of BLTP3A from lysosomes remain unknown. BLTP3A dissociation was not due to loss of Rab7 binding sites on lysosomes as the binding of VPS13C requires active Rab7 at these organelles (Wang et al., 2024a). Likewise dissociation was not due to the rapid phosphorylation of Rab7 at serine 72, a process primarily mediated by the kinase activity of LRRK1 (Wang et al., 2024a) with an additional variable contribution of the kinase TBK1 (Nirujogi et al., 2021; Fujita et al., 2022; Heo et al., 2018; Talaia et al., 2024), as over-expression of a dominant-protein kinase active LRRK1 mutant (GFP-$LRRK1^{K746G}$) did not affect the localization of BLTP3A-mRFP foci next to lysosomes in RPE-1 cells (**Supplemental Figure 1F & Supplemental Figure 1H**).

CASM-dependent reassociation of BLTP3A with the lysosomal membrane after its LLOMe induced rapid dissociation

One event triggered by LLOMe-dependent damage of the lysosomal membrane is activation of CASM (Conjugation of Atg8 to Single Membranes) (Durgan and Florey, 2022; Boyle et al., 2023; Corkery et al., 2023; Kaur et al., 2023; Fischer et al., 2020). This is the process whereby lysosome perturbations that drive V-ATPase V0-V1 association in their membrane to enhance its proton pump activity also result in the recruitment of a subset of components of the classical autophagy pathway resulting in the lipidation and recruitment to the lysosomal membrane of mATG8 family proteins. These are small adaptors that are recruited to membranes in response to their triggered conjugation to PE or PS and bind proteins which contain the so-called LC3-interacting region (LIR) motif, typically found in disordered protein regions. Atg8 family proteins, which comprise six

358 members in mammals, are well established players in conventional autophagy (Melia et al., 2020;
359 Nieto-Torres et al., 2021; Figueras-Novoa et al., 2024; Deretic et al., 2024): they interact with the
360 isolation membrane via their lipid tail and recruit cargo targeted for autophagy via their LIR-motif-
361 dependent interactions. However, the discovery of CASM has now revealed another important
362 role of these proteins which is being intensely investigated (Durgan and Florey, 2022).
363
364 In view of the identification of two mATG8 proteins, MAP1LC3B and GABARAP, as interactors of
365 BLTP3A (**Figure 3C**), we further explored a potential role of CASM in BLTP3A dynamics. A search
366 for LIR motifs in BLTP3A using the publicly available iLR Autophagy Database
367 (https://ilir.warwick.ac.uk/index.php) predicts such a motif [Position Specific Scoring Matrix
368 (PSSM) score: 16] within a disordered loop projecting out from the C-terminal region of BLTP3A,
369 but not of BLTP3B, from several mammalian species, including humans (aa 1129-1134) (**Figure**
370 **5A**) (see also (Tu and Brumell, 2020)). The high degree of conservation of this motif relative to its
371 surrounding a.a. sequences suggests its physiological importance, consistent with our co-affinity
372 purification results. Moreover, structure-prediction algorithms (Abramson et al., 2024) predict with
373 high confidence an interaction between the LIR motif of BLTP3A and the majority of the six known
374 mATG8 proteins (**Supplemental Figure 2D & 2E**).
375
376 To determine a potential physiological role of an mATG8-BLTP3A interaction, we co-expressed
377 BLTP3A-mRFP and GFP-LC3B in RPE-1 cells. The localization of BLTP3A-mRFP on lysosomes
378 and to large accumulations was not changed by the over-expression of GFP-LC3B, which was
379 mostly cytosolic (**Figure 5B**). Starvation of these cells resulted in the formation of GFP-LC3B-
380 positive foci, as expected, but did not alter the localization of BLTP3A-mRFP, indicating that
381 BLTP3A does not play a role in conventional autophagy (**Figure 5B**).
382
383 We next monitored the response of LC3B relative to BLTP3A after addition of LLOMe. In the first
384 few minutes after LLOMe addition, when BLTP3A-mRFP as described above dissociated from
385 lysosomes, GFP-LC3B fluorescence remained cytosolic with no overlap with the BLTP3A
386 fluorescence (**Figure 5C**). After ~5-10 mins of LLOMe treatment, however, GFP-LC3B began to
387 accumulate on the surface of some lysosomes (**Figure 5C**), as previously reported (Cross et al.,
388 2023), and this association correlated with the recruitment of a pool of BLTP3A-mRFP to such
389 lysosomes, consistent with BLTP3A being an mATG8 effector. Similar results were observed
390 upon addition of the lysosome stressor glycyl-L-phenylalanine 2-naphthylamide (GPN)
391 (**Supplemental Figure 3**) (Chen et al., 2024; Durgan and Florey, 2022), another CASM activator.
392 Deletion of the LIR motif of BLTP3A (BLTP3AΔLIR-mRFP) did not affect the localization of
393 BLTP3A in the absence of LLOMe treatment and did not abolish the shedding of BLTP3A upon
394 LLOMe treatment but abolished its recruitment to GFP-LC3B positive lysosomes after LLOMe
395 (**Figure 5D**), demonstrating that the LIR motif of BLTP3A is necessary for such recruitment. The
396 reassociation of BLTP3A with lysosomes occurred along the entire surface of lysosomes,
397 mirroring the localization of LC3. Moreover, this BLTP3A pool was not associated with vesicles
398 as determined by CLEM of BLTP3A-mRFP and GFP-LC3B positive lysosomes in RPE-1 cells
399 after 15 mins of LLOMe exposure (**Figure 5E**), which revealed a lack of vesicles in the presence
400 of these lysosomes. These findings indicate that the LIR motif-dependent association of the C-

401 terminal region of BLTP3A with lysosomes is mutually exclusive with the association of BLTP3A
402 with vesicles, which, as mentioned above, also involves this region of the protein.
403
404 Collectively, these results suggest that the orientation of BLTP3A mediated by its LIR domain at
405 the lysosome surface is likely opposite to the one mediated by Rab7 (**Figure 5F**). The binding
406 mediated by the LIR domain would leave the N-terminal, chorein domain region of BLTP3A
407 available for binding to the ER.
408
409 **DISCUSSION**
410
411 Our study shows that BLTP3A, a protein expected to transport lipids between adjacent
412 membranes via a bridge-like mechanism, is a component of protein networks implicated in
413 membrane traffic in late endosomes/lysosomes and that lysosome damage has an impact on its
414 localization. BLTP3A can bind and cluster vesicles of the endocytic system positive for VAMP7
415 and VAMP4 and tether them to lysosomes via an interaction of its N-terminal region with
416 lysosome-bound Rab7. Upon lysosome membrane damage and recruitment to their surface of
417 mATG8 family proteins via CASM, this Rab7-dependent interaction is lost. However, within
418 minutes BLTP3A then reassociates with damaged lysosomes by interacting with mATG8 proteins
419 via a LIR motif present in its C-terminal region which is no longer bound to vesicles. As we discuss
420 below, we suggest that this second interaction is the one relevant for lipid transport, and that
421 BLTP3A may cooperate with other BLTPs in the response of cells to lysosome damage.
422
423 The property of BLTP3A to associate with small vesicles and induce their striking accumulation
424 when overexpressed is shared with BLTP3B (Hanna et al., 2022). Moreover, BLTP3A- and
425 BLTP3B-positive vesicles have similar size, share at least one cargo, ATG9A, and clusters of
426 them are closely associated to other organelles, Rab5 positive early endosomes in the case of
427 BLTP3B and Rab7 positive lysosomes in the case of BLTP3A. However, they also differ at least
428 partially in protein composition, as only BLTP3A positive clusters are strongly immunolabeled by
429 antibodies directed against VAMP7 and VAMP4. The known role of VAMP7 in membrane traffic
430 at late stages of the endolysosomal pathway (Advani et al., 1999) is in agreement with the
431 localization of BLTP3A positive vesicles next to lysosomes.
432
433 Both VAMP7 and VAMP4 were reported to directly bind via their longin domain to a small N-
434 terminal motif present the Parkinson disease protein LRRK2 and its paralogue LRRK1 (Wang et
435 al., 2018; Filippini et al., 2023). It was therefore of interest that in some cells a striking
436 colocalization was observed between both LRRK1 and LRRK2 with vesicle clusters induced by
437 BLTP3A overexpression, although why such a striking colocalization was observed only in a
438 subset of cells remains unclear. Evidence that both LRRK1 and LRRK2 have a role in lysosome
439 biology makes a potential functional link between them and BLTP3A plausible. Interestingly,
440 proteomics studies of the impact of LRRK2 and its kinase activity on protein levels in lungs have
441 identified among major alterations changes in the levels of Rab27A, Rab27B, melanophilin, and
442 Rab45 (D. Alessi, Dundee, UK, personal communication) proteins that our present study has
443 linked to BLTP3A biology, although mechanistic aspects remain to be elucidated.
444

BLTP3 vesicle clusters are reminiscent of the clusters of synaptic vesicles at synapses. Such clusters were shown to have the properties of liquid biomolecular condensates (Milovanovic and De Camilli, 2017; Milovanovic et al., 2018; Park et al., 2021). Similarly, vesicle clusters involving BLTP3A and BLTP3B are very dynamic (see for example the fission of these clusters in (Hanna et al., 2022)). The assembly of BLTP3A-positive vesicle clusters and their anchorage to endosomes/lysosomes, implies a minimum of three direct or indirect interactions of BLTP3A: 1) an interaction with vesicles to capture them, 2) an interaction with itself or with adaptor proteins to cluster vesicles and 3) an interaction with lysosomes to account for the anchoring of the vesicle clusters to these organelles. We have shown that the interaction with lysosomes of vesicle-associated BLTP3A (interaction #3) is mediated by the binding to lysosome-bound Rab7, consistent with its being a Rab7 effector. Moreover, our results suggest that such an interaction involves the N-terminal region of BLTP3A, where we have detected the Rab7 binding site. We have also shown that the binding to vesicles (interaction #1) is mediated by the opposite end of the protein, i.e. its C-terminal region, but so far, we have not detected a binding partner.

We note that even in the case of synaptic vesicle condensates, which involve interactions between synapsin (a cytosolic protein), and synaptophysin (a vesicle protein), a direct interaction between the two proteins could not be detected by co-affinity purification (Südhof et al., 1989; De Camilli et al., 1990; Clayton and George, 1998), although clearly such an interaction occurs in living cells where low affinity is counteracted by multivalency: a multiplicity of low affinity interactions between synapsin with itself and with synaptophysin, a protein present in multiple copies on the vesicles. Concerning the mechanisms responsible for vesicle clustering (interaction #2), these may involve self-association of BLTP3A via low complexity unfolded sequences that project out of its rod-like core, or binding of BLTP3A to yet to be discovered adaptor/crosslinker proteins. As the property to cluster vesicles is shared by both BLTP3A and BLTP3B, such a property must rely on shared molecular determinants of these two proteins. Ongoing work is addressing these mechanisms. The property of BLTP3 proteins to cluster vesicles into small packages may be an important aspect of their physiological function as BLTP3B-positive vesicles were shown to be organized in small clusters even at physiological levels of expression (Hanna et al., 2022). Large clusters likely result from BLTP3 overexpression, although other scenarios, such as that BLTP3 overexpression may result in vesicle accumulation due to a dominant negative effect on their fusion with downstream targets, cannot be ruled out.

Our study indicates that the Rab7-dependent association of BLTP3A with lysosomes requires a portion of BLTP3A located in proximity of its N-terminal region, the so-called chorein motif (Kumar et al., 2018). In most other BLTP family members, the chorein or chorein-like motifs are localized at the ER, which is typically thought to be the “donor” membrane in their lipid transport function (Leonzino et al., 2021; Dziurdzik and Conibear, 2021; Wong et al., 2019). This is also the case for VPS13C, another Rab7 effector, which binds Rab7 on lysosomes via its C-terminal moiety. Thus, we consider it unlikely that the orientation of BLTP3A when cross-linking vesicles to Rab7 may be relevant to its lipid transport properties. Some potential insight about a bridge-like lipid transfer function of BLTP3A came from analysis of the response of BLTP3A to lysosome damage.

Lysosomal membrane damage activates multiple response mechanisms at timepoints ranging from seconds to hours (Skowyra et al., 2018; Radulovic et al., 2018; Meyer and Kravic, 2024). Conjugation of mATG8 proteins to the surface of lysosomes (CASM pathway) is one such response (Durgan and Florey, 2022). mATG8 proteins can be detected on lysosomes ~10 mins after the initiation of membrane damage, similar to the time frame of BLTP3A reassociation. It is therefore of great interest that 1) top hits identified from our immunoprecipitation of endogenously tagged BLTP3A^V5 from A549 cells are two mATG8 proteins (MAP1LC3B and GABARAP) and 2) BLTP3A contains a LIR motif (i.e. an Atg8 binding consensus) within a disordered loop projecting out of the C-terminal rod-like region. Accordingly, we found that the reassociation of BLTP3A follows the accumulation of LC3B on the surface of lysosomes and that the LIR motif is required for the reassociation of BLTP3A with lysosomes after LLOMe treatment.

The C-terminal region of BLTP3A, where the LIR motif is localized, is near the region expected to bind vesicles. Importantly, the pool of BLTP3A that reassociates with the lysosomal surface is not bound to small vesicles, although clusters of BLTP3A positive vesicles persist in the cytoplasm, suggesting that the LIR motif-dependent interaction of BLTP3A with lysosome-bound LC3B is mutually exclusive, possibly because of steric hindrance or regulatory mechanisms, with its association with vesicles. A binding of BLTP3A to lysosomes via its LIR motif would leave its N-terminal chorein domain region free to interact with the ER (**Figure 5F**).

Lysosome membrane damage also results in the formation of ER-lysosome tethers comprising other lipid transport proteins, such as ORP proteins (Tan and Finkel, 2022; Radulovic et al., 2022), VPS13C (Wang et al., 2024a) and ATG2 (Tan and Finkel, 2022; Cross et al., 2023), most likely as a cellular response aimed at protecting or repairing membranes by delivering new lipids. (Interestingly, while ATG2 also contain a LIR motif, its recruitment to lysosomes, in contrast to the recruitment of BLTP3A, does not require this motif (Cross et al., 2023)). We suggest that under these conditions, close appositions between lysosomes and the ER allow the N-terminal chorein domain of BLTP3A, which is no longer engaged by Rab7 at the lysosomal surface, to interact with the ER, thus allowing the formation of BLTP3A-dependent ER-to-lysosome bridges that may cooperate with other BLTPs in delivering membrane lipids from the ER to lysosomes.

In conclusion, our study links BLTP3A to the function of late endosomes and lysosomes and suggests that one of its functions is to cooperate in the response to lysosome damage as an effector of CASM. As lysosomes play a key role in cells of the immune system, it is of special interest that several coding variants of BLTP3A are associated with susceptibility to systemic lupus erythematosus (SLE) (Gateva et al., 2009; Zhang et al., 2011; Wen et al., 2020), a chronic autoimmune disease.

MATERIALS AND METHODS

Antibodies and Reagents

The list of plasmids, antibodies, their working dilution, and the supplier for this study can be found in the **Key Resource Table** at the following link:

https://docs.google.com/spreadsheets/d/1RVOPrz9L_QFf1PetDbkS3vPMHXVXI_QYCKIUzjgA3lc/edit?usp=sharing

Generation of Plasmids

All BLTP3A and BLTP3B ORFs used in this study utilized a human codon optimized sequence designed and purchased from Genscript. Codon optimized human BLTP3 chimeras were amplified using PCR from the pcDNA3.1 plasmid and ligated into a pmCh-N1 plasmid. Most constructs were generated with regular cloning protocols or through site-directed mutagenesis. The desired ORFs were amplified by PCR and inserted into plasmids through enzyme digestions and ligation. Some amplified ORFs were ligated using HiFi assembly (NEB). Details of primer sets, enzymes, techniques, and plasmids used for each construct can be found in the **Key Resource Table**.

Detailed protocol for the molecular cloning of BLTP3 plasmids for expression in mammalian cells is at: https://dx.doi.org/ 10.17504/protocols.io.8epv5z5kjv1b/v1

Correlative Light and Electron Microscopy

For TEM CLEM, RPE-1 cells were plated on 35 mm gridded, glass-bottom MatTek dish (P35G-1.5-14-CGRD) and transfected as described above with BLTP3A-mRFP, LAMP1-GFP, mito-BFP. Cells were pre-fixed in 4% PFA in dPBS then washed with dPBS before fluorescence light microscopy imaging. Regions of interest were selected and their coordinates on the dish were identified using phase contrast. Cells were further fixed with 2.5% glutaraldehyde in 0.1 M sodium cacodylate buffer, postfixed in 2% OsO_4 and 1.5% $K_4Fe(CN)_6$ (Sigma-Aldrich) in 0.1 M sodium cacodylate buffer, *en bloc* stained with 2% aqueous uranyl acetate, dehydrated in graded series of ethanols (50%, 75%, and 100%), and embedded in Embed 812. Cells of interest were relocated based on the pre-recorded coordinates. Ultrathin sections (50-60 nm) were post-stained with uranyl acetate substitute (UranyLess, EMS), followed by a lead citrate solution. Sections were observed in a Talos L 120C TEM microscope at 80 kV, images were taken with Velox software and a 4k × 4K Ceta CMOS Camera (Thermo Fisher Scientific). Except noted all reagents were from EMS (Electron Microscopy Sciences), Hatfield, PA.

Detailed protocol for 2D TEM CLEM is at:
https://dx.doi.org/10.17504/protocols.io.261gend2jg47/v1

Cell culture and Transfections

hTERT-RPE-1 cells were a kind gift of A. Audhya (University of Wisconsin, Madison, WI). A549 and COS-7 cells were obtained from ATCC. All mammalian cells were maintained at 37ºC in humidified atmosphere at 5% CO_2 unless noted otherwise. A549 and COS-7 cells were grown in DMEM and RPE-1 cells in DMEM/F12 medium (Thermo Fisher Scientific) supplemented with 10% FBS, 100 U/mL penicillin, 100mg/mL streptomycin. 2mM glutamax (Thermo Fisher Scientific) was

575 added to all media for RPE-1 cells. All cell lines were routinely tested and always resulted free
576 from mycoplasma contamination.
577
578 Transient transfections were carried out on cells that were seeded at last 8 h prior. All
579 transfections of plasmids used FuGENEHD (Promega) to manufacturers specifications for 16-24
580 h in complete media without antibiotics.
581
582 Detailed protocol for cell culture, transfection, immunocytochemistry, and imaging:
583 https://dx.doi.org/10.17504/protocols. io.eq2lyp55mlx9/v1
584
585 **Immunoblotting and Imaging Procedure**
586
587 All cell samples analyzed by immunoblotting were scraped from plates and harvested by
588 centrifugation (500xg for 5 minutes). The pellet was washed with ice-cold dPBS and centrifuged
589 again in a 1.7mL Eppendorf tube. The cell pellet was resuspended in Lysis buffer (20mM Tris-
590 HCl pH 7.5, 150mM NaCl, 1% SDS, 1mM EDTA) containing protease inhibitor cocktail (Roche).
591 The lysate was clarified by centrifugation (17,000xg for 10 minutes) and a small portion of lysate
592 was reserved for quantification of protein concentration by Bradford. The remaining lysate was
593 then mixed with 5x SDS sample buffer (Cold Spring Harbor) to 1x concentration and then heated
594 to 95°C for 3 minutes. 15-25ug of protein samples were separated by electrophoresis on a 4-20%
595 Mini-PROTEAN TGX gel and then subjected to standard western blot transfer and procedures.
596 Blots were imaged using the Odyssey imaging system (LI-COR) using manufacturers protocols.
597 All primary antibodies used in this study are listed in the **Key Resource Table**.
598
599 **Mouse tissue lysate preparation**
600
601 Tissues were collected from sacrificed WT C57BL/6J mice (Jackson Laboratory strain #000664).
602 For each 1 g of material, 10 ml of buffer (25 mM Hepes, pH 7.4, 200 mM NaCl, 5% glycerol,
603 protease inhibitors) was added. Mechanical lysis was performed using a glass dounce-
604 homogenizer (15 strokes). Triton X-100 was added to 1%, and material was rotated at 4°C for 30
605 min. Material was centrifuged at 1,000 g to remove cell debris and the collected supernatant was
606 centrifuged at 27,000 g for 20 min. The resulting supernatant mixed was flash frozen and stored
607 at −80°C until use.
608
609 **Live Cell Imaging and Immunofluorescence**
610
611 For all live cell microscopy cells were seeded on glass-bottom mat-tek dishes (MATtek
612 corporation) 5500/cm^2 in complete media. Transfections were carried out as described above.
613 Spinning-disk confocal imaging was preformed 16-24 h post transfection using an Andor Dragon
614 Fly 200 (Oxford Instruments) inverted microscope equipped with a Zyla cMOS 5.5 camera and
615 controlled by Fusion (Oxford Instruments) software. Laser lines used: DAPI, 440nm; GFP, 488;
616 RFP, 561; Cy5, 647. Images were acquired with a PlanApo objective (60x 1.45-NA). During
617 imaging, cells were maintained in Live Cell Imaging buffer (Life Technologies) in a cage incubator
618 (Okolab) with humidified atmosphere at 37°C. LLOMe (Sigma-Aldrich, CAS: 1668914-8) and GPN

619 (Cayman Chemical, CAS: 14634) were dissolved in ethanol and used at a final concentration of
620 1 mM for all imaging experiments. All live imaging experiments are representative of at least 10
621 independent repeats.
622
623 Immunofluorescent experiments were performed with cells grown on #1.5 glass cover slips. Cells
624 were fixed with 4% PFA in PBS (Gibco, 14190144) for 15 mins at room temperature, washed 3x
625 with PBS, permeabilized using antibody dilution buffer (1x PBS containing 0.2% saponin and 2%
626 BSA) at 4°C overnight with the indicated primary antibodies. Slides were washed three times with
627 PBS containing 0.02% saponin to remove excess primary antibody and subsequently incubated
628 with secondary antibodies diluted in antibody dilution buffer for 45 min at room temperature in the
629 dark. Slides were washed again three times to remove secondary antibody with PNS containing
630 0.02% saponin prior to mounting.
631
632 **Generation of CRISPR edited Cell Lines**
633
634 Endogenous tagging of A549 cells was carried out using a CRISPR/Cas9 ribonucleoprotein
635 (RNP) complex. Commercially purified Cas9 nuclease (IDT) was combined and incubated with
636 trans-activating CRISPR RNA (tracrRNA) and a BLTP3A-targeting guide RNA to form the RNP
637 complex. The RNP complex was then incubated with a single-stranded repair template containing
638 the insert sequence and ultimately delivered to A549 cells via electroporation. Subsequently, the
639 RNP-transfected pools were serially diluted and plated at 1 cell per well on a glass bottom 96-
640 well plate. Wells were expanded and tested for editing via PCR until an appropriate number of
641 edited clones were obtained. All gRNAs used in this study are listed in the **Key Resource Table**.
642
643 **Immunoprecipitation of endogenously tagged BLTP3A**
644
645 Wild-type or endogenously edited A549 cells expressing BLTP3A^V5 were grown to 90%
646 confluency on 15 cm plates (Falcon). Two 15 cm plates were used for each independent replicate
647 of wild-type and edited cells (n=3). Cells were washed with dPBS (Gibco) and then scrapped from
648 the surface of the plates into 2 mL of dPBS per plate. Cells were pelleted at 1000g for 5 min and
649 the dPBS supernatant was removed. Cells were resuspended in 2 mL of ice-cold lysis buffer (50
650 mM Tris pH 7.6, 150 mM NaCl, 1% Triton X-100, protease inhibitors [Roche]) and rotated at 4°C
651 for 20 mins. Cell lysates were spun at 17000g for 10 mins to clear insoluble material. The
652 supernatants were then added to 75 uL (slurry) of anti-V5 magnetic resin (ChromoTek) and let
653 rotate at 4°C for 2 hrs. Resin was washed twice for 5 mins rotating with ice cold lysis buffer and
654 then washed a third time without detergent for 5 mins (50 mM Tris pH 7.6, 150 mM NaCl, protease
655 inhibitors). Supernatant was removed and resin was stored at −80°C.
656
657 **Proteomics analyses**
658
659 **Protein digestion**
660 The beads were resuspended in 80 µL of 2M Urea, 50 mM ammonium bicarbonate (ABC) and
661 treated with DL-dithiothreitol (DTT) (final concentration 1 mM) for 30 minutes at 37°C with shaking
662 at 1100 rpm on a Thermomixer (Thermo Fisher). Free cysteine residues were alkylated with 2-

663 iodoacetamide (IAA) (final concentration 3.67 mM) for 45 minutes at 25°C with shaking at 1100
664 rpm in the dark. The reaction was quenched using DTT (final concentration 3.67 mM), and LysC
665 (750 ng) was added, followed by incubation for 1h at 37°C at 1150 rpm. Finally, trypsin (750 ng)
666 was added, and the mixture was incubated for 16 hours at 37°C with shaking at 1150 rpm.
667
668 After incubation, an additional 500 ng of trypsin was added to the sample, followed by a 2-hour
669 incubation at 37°C at 1150 rpm. The digest was then acidified to pH <3 by adding 50%
670 trifluoroacetic acid (TFA), and the peptides were desalted on C18 stage tips (Empore C18
671 extraction disks). Briefly, the stage tips were conditioned with sequential additions of: i) 100 μL
672 methanol), ii) 100 μL 70% acetonitrile (ACN)/0.1% TFA, iii) 100 mL 0.1% TFA twice. After
673 conditioning, the acidified peptide digest was loaded onto the stage tip, and the stationary phase
674 was washed with 100 μL 0.1% formic acid (FA) twice. Finally, the peptides were eluted with 50
675 μL 70% ACN/0.1% FA twice. Eluted peptides were dried under vacuum in a Speed-Vac
676 centrifuge, reconstituted in 12 μL of 0.1% FA, sonicated and transferred to an autosampler vial.
677 Peptide yield was quantified using a NanoDrop (Thermo Fisher).
678
679 **Mass spectrometry analyses**
680 Peptides were separated on a 25 cm column with a 75 μm diameter and 1.7 μm particle size,
681 composed of C18 stationary phase (IonOpticks Aurora 3 1801220) using a gradient from 2% to
682 35% Buffer B over 90 minutes, followed by an increase to 95% Buffer B for 7 minutes (Buffer A:
683 0.1% FA in HPLC-grade water; Buffer B: 99.9% ACN, 0.1% FA) with a flow rate of 300 nL/min on
684 a NanoElute2 system (Bruker).
685
686 MS data were acquired on a TimsTOF HT (Bruker) with a Captive Spray source (Bruker) using a
687 data-independent acquisition PASEF method (dia-PASEF). The mass range was set from 100 to
688 1700 *m/z*, and the ion mobility range from 0.60 V.s/cm^2 (collision energy 20 eV) to 1.6 V.s/cm^2
689 (collision energy 59 eV), a ramp time of 100 ms, and an accumulation time of 100 ms. The dia-
690 PASEF settings included a mass range of 400.0 to 1201.0 Da, mobility range 0.60-1.60, and an
691 estimated cycle time of 1.80 seconds. The dia-PASEF windows were set with a mass width of
692 26.00 Da, mass overlap 1.00 Da, and 32 mass steps per cycle.
693
694 **DIA Data Analysis**
695 Raw data files were processed using Spectronaut version 17.4 (Biognosys) and searched with
696 the PULSAR search engine against the Homo sapiens UniProt protein database (226,953 entries,
697 downloaded on 2022/09/23). Cysteine carbamidomethylation was set as fixed modifications,
698 while methionine oxidation, acetylation of the protein N-terminus, and deamidation (NQ) were
699 defined as variable modifications. A maximum of two trypsin missed cleavages was allowed.
700 Searches used a reversed sequence decoy strategy to control the peptide false discovery rate
701 (FDR), with a 1% FDR threshold for identification. An unpaired t-test was used to calculate p-
702 values for differential analysis, and volcano plots were generated based on log2 fold change and
703 q-value (multiple testing corrected p-value). A q-value of ≤0.05 was considered the statistically
704 significant cut-off.
705

706 The mass spectrometry proteomics data have been deposited to the ProteomeXchange
707 Consortium via the PRIDE partner repository with the dataset identifier PXD056338.
708
709 **Image processing, Analysis, and Statistics**
710
711 Florescence images presented in this study are representative of cells imaged in at least three
712 independent experiments and were processed with ImageJ software. The dimensions of some of
713 the magnification insets or panels were enlarged using the *Scale* function on ImageJ.
714
715 Statistical analysis was performed with GraphPad Prism 10 software. Groups were compared
716 using a two-tail unpaired Student *t* test and results were deemed significant when a p value was
717 smaller than 0.05.
718
719 **ACKNOWLEDGMENTS**
720
721 We thank Thomas Melia and Shawn Ferguson (Yale) for discussion and advice, James Liu
722 (Janelia Res Labs) for advice on endogenous tagging, Dario Alessi (Dundee, UK) for the personal
723 communication of unpublished data and Chase Amos and Hanieh Falahati for critical reading of
724 the manuscript. This work was supported in part by the NIH (DA018343 and NS36251), by
725 Aligning Science Across Parkinson's (ASAP-000580) through the Michael J. Fox Foundation for
726 Parkinson's Research (MJFF) to PDC, and the MSK Cancer Center Support Grant/Core Grant
727 (P30 CA008748).
728
729
730 **FIGURE LEGENDS**
731
732 **Figure 1: Endogenous and exogenous BLTP3A form accumulations that associate with**
733 **lysosomes.**
734
735 **(A)** AlphaFold prediction of full-length BLTP3A with ConSurf conservation scores (top left) for
736 each a.a. or cross-section of surface rendering of BLTP3A channel (top right) highlighting
737 hydrophobic residues (orange). Linear representation of BLTP3A: per residue ConSurf scores
738 (top) and RBG organization (bottom). IDR, predicted intrinsically disordered region (light gray);
739 CH, C-terminal helix (dark gray).
740 **(B)** Alignment of the a.a. of motifs important for the indicated protein interactions of BLTP3B with
741 corresponding sequences of BLTP3A. ConSurf conservation scores for each a.a. is indicated by
742 color (same color scheme as in Fig.1A)
743 **(C)** Western blot of lysates of wild-type mouse tissues for BLTP3A, BLTP3B, and vinculin as a
744 loading control.
745 **(D)** Western blot of control and edited (BLTP3A^V5) cell clones for BLTP3A, V5, and alpha-tubulin
746 as a loading control.
747 **(E)** Fluorescence images of endogenously edited (left) or parental control (middle) A549 cells with
748 antibodies against LAMP1 (green) and V5 (magenta). Scale bar, 10 µm. The insets are a zoom
749 of a small region of the cell. Scale bar, 1 µm. Right: Fluorescence of exogenous BLTP3A-GFP

750 (green) in endogenously edited A549 cell. Scale bar, 5 µm. Insets: zoom of square region of cell
751 showing co-localization of endogenous BLTP3A^V5 signal from immunolabeling with antibodies
752 against V5 (magenta) and BLTP3A-GFP fluorescence (green). Scale bar, 1 µm.
753 **(F)** Fluorescence image of wild-type RPE-1 cell immunostained with antibodies against LAMP1
754 (green) and DAPI (blue). Scale bar, 5 µm.
755 **(G)** Fluorescence image of an RPE-1 cell expressing exogenous BLTP3A-mRFP (large field,
756 inverted grays) and LAMP1-GFP (not shown). Scale bar, 5 µm. The area enclosed by a dotted
757 rectangle is shown at right at high magnification with BLTP3A-mRFP in magenta and LAMP1-
758 GFP in green (individual channels are shown as inverted grays). Red arrows indicate large
759 BLTP3A accumulations not associated with lysosomes. Scale bar, 1 µm.
760 **(H)** CLEM of a BLTP3A-mRFP positive cluster in an RPE-1 cell. Left: florescence images of
761 BLTP3A-mRFP (magenta). Scale bar, 1 µm. Right: EM micrograph of the field shown at left
762 revealing that the BLTP3A-mRFP fluorescence reflects clusters of small vesicles, many of them
763 tethered to the surface of lysosomes. Scale bar, 500 nm.
764 **(I)** Distance between the membranes of lysosomes and tethered vesicles from EM micrographs.
765 Mean = 10.8 nm; standard error of the mean = ±0.20 nm.
766 **(J)** Left: Fluorescence image of an RPE-1 cell expressing exogenous BLTP3A-mRFP (inverted
767 grays) and immunolabeled with antibodies against VAMP7 (shown in the high mag fields at right).
768 Scale bar, 5 µm. Right: zooms of different RPE-1 cells expressing exogenous BLTP3A-mRFP
769 (magenta) and immunolabeled (green) with antibodies against the following endogenous proteins,
770 VAMP4 and ATG9A. Individual channels are shown as inverted grays. Merge of channels on
771 bottom. Scale bar, 1 µm.
772
773 **Figure 2: The N-terminus of BLTP3A associates with Rab7 on the surface of lysosomes.**
774
775 **(A)** Fluorescence images of RPE-1 cells expressing exogenous BLTP3A-mRFP (shown in
776 inverted grays) and (not shown) GFP-tagged wild type Rab7 (left) or dominant negative (DN)
777 Rab7 (T22N) (right). Scale bar, 5 µm.
778 **(B)** CLEM of a BLTP3A-mRFP positive cluster in an RPE-1 cell expressing GFP-tagged dominant
779 negative Rab7. Left: fluorescence image (magenta). Scale bar, 1 µm. Right: EM micrograph of
780 the field shown at left revealing that the BLTP3A-mRFP fluorescence reflects clusters of small
781 vesicles. Scale bar, 500 nm.
782 **(C)** BLTP3 chimeras design. Left: Surface representation of the predicted RBG core of BLTP3A.
783 Red and blue indicate positive and negative charges, respectively, and gray indicates
784 hydrophobic surfaces. Right: Surface representation (top) and ribbon representation (bottom) of
785 the "untwisted" protein showing individual RBG motifs. Bottom: Cartoon of chimeras consisting of
786 BLTP3A (dark orange) and BLTP3B (light orange) RBG motifs.
787 **(D)** High-magnification live fluorescence images of RPE-1 cells expressing the indicated BLTP3-
788 mRFP constructs (magenta) and LAMP1-GFP (green). Individual channels are shown as inverted
789 grays. Scale bar, 1 µm.
790 **(E)** Ribbon representation of the AlphaFold prediction of a.a. 1-336 of BLTP3A. Blue indicates
791 loops connecting adjoining RBG motifs, and gray indicates the first beta-stand of the third RBG
792 motif.

(F) Fluorescence images (inverted grays) of RPE-1 cells expressing BLTP3A-1-336-mRFP and either (not shown) GFP-Rab7 (left), or GFP-Rab7 T22N (right). Scale bar, 5 µm. A zoom of an area of the cell at left (dotted square) expressing BLTP3A-1-336-mRFP (magenta) is also shown, along with the Rab7 fluorescence (green), demonstrating the localization of BLTP3A-1-336-mRFP around the entire profile of lysosomes. Individual channels are shown as inverted grays. Scale bar, 2 µm.
(G) Cartoon depicting the proposed association of BLTP3A vesicle clusters with the surface of lysosomes and the dependence of this association on Rab7.

Figure 3: The C terminus of BLTP3A associates with vesicles

(A) Top: Linear representation of BLTP3A RBG organization and C-terminal truncations indicated by arrows. Bottom left: AlphaFold-based structure of the C terminus of BLTP3A channel. Individual residues are colored by conservation scores as Fig. 1A. Truncations are indicated by arrows. Bottom right: Fluorescence images (inverted grays) of RPE-1 cells expressing the indicated BLTP3A-mRFP constructs along with dominant negative Rab7 (not shown) demonstrating that the property of BLTP3A to bind and cluster vesicles is dependent on its region comprised between a.a. 1327 and 1364. Note that the construct 1-1327, shows a focal accumulation next to the nucleus, which is VAMP7 negative, likely reflecting its pool bound to Rab45 (see Supplemental Figure 1A). Scale bar, 5 µm. Zoomed images (dotted squares) are shown below the main field along with VAMP7 fluorescence. Scale bar, 1 µm.
(B) Western blots of cell extracts (inputs) of control and edited A549 cells, and of material immunoisolated from these extracts by anti-V5 magnetic beads. Immunolabeling for BLTP3A, V5 (endogenously tagged BLTP3A), and for GAPDH as a loading control, are shown.
(C) Scatter plot of mass spectrometry-identified proteins in immunoisolated material from either control or endogenously edited BLTP3A^V5 A549 cells using anti-V5 magnetic beads. Proteins significantly enriched in material immunoisolated form edited cells compared to wild type cells are plotted in the right-top quadrant. Proteins of note are labeled in magenta.

Figure 4: Exogenous BLTP3A is shed from the surface of lysosomes upon damage of their membranes.

(A) Time-series of live fluorescence images (inverted grays) of exogenous BLTP3A-GFP and mApple-IST1 before and after addition of LLOMe. Arrowheads (magenta) point to BLTP3A accumulations shed from lysosomes upon addition of LLOMe. Scale bar, 5 µm.
(B) Time-series of live fluorescence images of BLTP3A-1-336-mRFP (magenta) and the lysosomal marker NPC1-GFP (green). Fluorescence of individual channels is shown in inverted grays. Scale bar, 2 µm.

Figure 5: Activation of CASM recruits BLTP3A to the surface of damaged lysosomes through an interaction with mATG8 proteins.

(A) Alignment of the region of BLTP3A orthologues from different species centered on the a.a. region required for mATG8 binding in human BLTP3A. The alignment shows a high degree of

837 conservation of the key residues of the LC3-interacting (LIR) motif among several chordates and
838 also observed in flies.
839 **(B)** Live fluorescence images (inverted grays) of RPE-1 cells expressing BLTP3A-mRFP (top) or
840 GFP-LC3B (bottom) in either fed (left) or starved (right) conditions. Arrows (magenta) indicate
841 GFP-LC3B positive foci. Scale bar, 5 µm.
842 **(C)** Time-series of live fluorescence images (inverted grays) of exogenous BLTP3A-mRFP and
843 GFP-LC3B before and after addition of LLOMe. Arrowheads point to lysosomes where BLTP3A
844 and LC3B decorate the entire lysosome profile upon addition of LLOMe. Scale bar, 5 µm.
845 **(D)** Time-series of live fluorescence images (inverted grays) of exogenous BLTP3AΔLIR-mRFP
846 and GFP-LC3B before and after addition of LLOMe. Arrowheads point to lysosomes where LC3B,
847 but not BLTP3A lacking a LIR motif, decorates the entire lysosome profile upon addition of
848 LLOMe. Scale bar, 5 µm.
849 **(E)** CLEM of GFP-LC3B and BLTP3A-mRFP-positive lysosomes in an RPE-1 cell 15 min after
850 LLOMe addition. Left: Florescence image (inverted grays) of an RPE-1 cell expressing GFP-LC3B
851 and (not shown) BLTP3A-mRFP and mito-BFP, 15 min after addition of LLOMe. Scale bar, 5 µm.
852 Middle: High magnification of the RPE-1 cell at left (dotted square) showing both the BLTP3A-
853 mRFP (magenta) and the GFP-LC3B (green) channels. Individual channels are shown as inverted
854 grays. Scale bar, 2 µm. Right: EM image (scale bar, 500 nm) corresponding to the high
855 magnification fluorescence images (an asterisk and a pound sign mark the same lysosomes in
856 the fluorescence and EM images, respectively). Note absence of vesicles in spite of the presence
857 of BLTP3A fluorescence around the lysosomes.
858 **(F)** Hypothetical model illustrating the different organization and orientation of BLTP3A on the
859 surface of lysosomes depending on the state of the cell.
860
861
862 **SUPPLEMENTAL FIGURE LEGENDS**
863
864 **Supplemental Figure 1**
865
866 **(A)** Live fluorescence images (inverted grays) of RPE-1 cells expressing either GFP-Rab45 (left),
867 BLTP3A-mRFP (center), or both proteins together (only BLTP3A is shown) (right) as indicated.
868 Scale bar, 5 µm. High-magnification scale bar, 2 µm.
869 **(B)** Genomic sequence of the edited BLTP3A locus (insertion of the V5 epitope) in A549 cell.
870 Blue, small Gly-Ser linkers; green, V5 epitope sequence.
871 **(C)** AlphaFold prediction of BLTP3A. The site where the V5 epitope (V904) was inserted is
872 indicated. The long disordered sequence and the C-terminal helix are shown in gray.
873 **(D)** Left: Fluorescence image of an RPE-1 cell expressing exogenous BLTP3B-mRFP (inverted
874 grays) and immunolabeled with antibodies against endogenous VAMP7 (shown at right in the
875 high magnification of the squared region in the main field). Scale bar, 5 µm. Right: zooms of
876 different RPE-1 cells expressing exogenous BLTP3B-mRFP (magenta) and immunolabeled with
877 antibodies (green) against endogenous VAMP4 or ATG9A. Individual channels are shown as
878 inverted grays. Merge of channels on bottom. Scale bar, 1 µm.
879 **(E)** Live fluorescence image of RPE-1 cell expressing exogenous RFP-LRRK1^{K746G} (green), which
880 is primarily cytosolic. Scale bar, 5 µm.

881 **(F)** Live fluorescence images (inverted grays) of RPE-1 cells expressing exogenous GFP-
882 LRRK1^{K746G} (left) and BLTP3A-mRFP (right). Scale bar, 10 µm. High magnifications of areas of
883 overlap (orange box) or no overlap (blue box) of the fluorescence of exogenous LRRK1 (green)
884 and BLTP3A (magenta) are shown at right. Scale bar, 2 µm.
885 **(G)** RPE-1 cell expressing BLTP3A-mRFP, GFP-LRRK1^{K746G} and mito-BFP. CLEM of a BLTP3A-
886 mRFP and GFP-LRRK1^{K746G} positive region showing abundance of small vesicles associated with
887 lysosomes in the corresponding EM image. The mito-BFP fluorescence is not shown and was
888 used for alignment. Scale bar, 2 µm for the fluorescence and 500 nm for the EM).
889 **(H)** Western blot of lysate of RPE-1 cells expressing exogenous RFP-LRRK1^{K746G} or RFP-
890 LRRK1^{D1409A} for RFP (to detect LRRK1 fusions), Rab7, phospho-Rab7 S72, and alpha-tubulin as
891 a loading control.
892
893 **Supplemental Figure 2**
894
895 **(A)** Live fluorescence image (inverted grays) of RPE-1 cells expressing GFP-LRRK2 (left) and
896 BLTP3A-mRFP (right). Scale bar, 10 µm. High magnifications of areas of overlap (orange box) or
897 no overlap (blue box) of the LRRK2 (green) and BLTP3A (magenta) fluorescence. Scale bar, 2
898 µm.
899 **(B)** Live fluorescence image (inverted grays) of COS7 cells expressing GFP-LRRK2 (left) and
900 BLTP3A-mRFP (right). Scale bar, 5 µm. High magnifications of areas of overlap (orange box) or
901 no overlap (blue box) of the LRRK2 (green) and BLTP3A (magenta) fluorescence. Scale bar, 2
902 µm.
903 **(C)** Fluorescence images of RPE-1 cells expressing the indicated BLTP3A-mRFP construct.
904 Scale bar, 5 µm
905 **(D)** AlphaFold3 multimer prediction of full-length MAP1LC3B (green) and a.a. 1110-1150 of
906 BLTP3A (magenta). Arrows indicate key residues of the LIR motif of BLTP3A.
907 **(E)** AlphaFold3 multimer predictions of mATG8 proteins and aa 1110-1150 of BLTP3A with and
908 without the LIR motif (ΔLIR).
909
910 **Supplemental Figure 3**
911
912 Time-series of live fluorescence images (inverted grays) of BLTP3A-mRFP and GFP-LC3B before
913 and after addition of GPN. Arrowheads point to lysosomes where BLTP3A and LC3B decorate
914 the entire profile upon addition of GPN. Time, seconds. Scale bar, 5 µm.
915

REFERENCES

Abramson, J., J. Adler, J. Dunger, R. Evans, T. Green, A. Pritzel, O. Ronneberger, L. Willmore, A.J. Ballard, J. Bambrick, S.W. Bodenstein, D.A. Evans, C.-C. Hung, M. O'Neill, D. Reiman, K. Tunyasuvunakool, Z. Wu, A. Žemgulytė, E. Arvaniti, C. Beattie, O. Bertolli, A. Bridgland, A. Cherepanov, M. Congreve, A.I. Cowen-Rivers, A. Cowie, M. Figurnov, F.B. Fuchs, H. Gladman, R. Jain, Y.A. Khan, C.M.R. Low, K. Perlin, A. Potapenko, P. Savy, S. Singh, A. Stecula, A. Thillaisundaram, C. Tong, S. Yakneen, E.D. Zhong, M. Zielinski, A. Žídek, V. Bapst, P. Kohli, M. Jaderberg, D. Hassabis, and J.M. Jumper. 2024. Accurate structure prediction of biomolecular interactions with AlphaFold 3. *Nature*. 630:493–500. doi:10.1038/s41586-024-07487-w.

Adlakha, J., Z. Hong, P. Li, and K.M. Reinisch. 2022. Structural and biochemical insights into lipid transport by VPS13 proteins. *Journal of Cell Biology*. 221:e202202030. doi:10.1083/jcb.202202030.

Advani, R.J., B. Yang, R. Prekeris, K.C. Lee, J. Klumperman, and R.H. Scheller. 1999. Vamp-7 Mediates Vesicular Transport from Endosomes to Lysosomes. *Journal of Cell Biology*. 146:765–776. doi:10.1083/jcb.146.4.765.

Anding, A.L., C. Wang, T.-K. Chang, D.A. Sliter, C.M. Powers, K. Hofmann, R.J. Youle, and E.H. Baehrecke. 2018. Vps13D Encodes a Ubiquitin-Binding Protein that Is Required for the Regulation of Mitochondrial Size and Clearance. *Current Biology*. 28:287-295.e6. doi:10.1016/j.cub.2017.11.064.

Armon, A., D. Graur, and N. Ben-Tal. 2001. ConSurf: an algorithmic tool for the identification of functional regions in proteins by surface mapping of phylogenetic information1. *Journal of Molecular Biology*. 307:447–463. doi:10.1006/jmbi.2000.4474.

Bahadoran, P., E. Aberdam, F. Mantoux, R. Buscà, K. Bille, N. Yalman, G. de Saint-Basile, R. Casaroli-Marano, J.-P. Ortonne, and R. Ballotti. 2001. Rab27a: A Key to Melanosome Transport in Human Melanocytes. *Journal of Cell Biology*. 152:843–850. doi:10.1083/jcb.152.4.843.

Baldwin, H.A., C. Wang, G. Kanfer, H.V. Shah, A. Velayos-Baeza, M. Dulovic-Mahlow, N. Brüggemann, A. Anding, E.H. Baehrecke, D. Maric, W.A. Prinz, and R.J. Youle. 2021. VPS13D promotes peroxisome biogenesis. *Journal of Cell Biology*. 220:e202001188. doi:10.1083/jcb.202001188.

Bentley-DeSousa, A., and S.M. Ferguson. 2023. A STING-CASM-GABARAP Pathway Activates LRRK2 at Lysosomes. 2023.10.31.564602. doi:10.1101/2023.10.31.564602.

Boyle, K.B., C.J. Ellison, P.R. Elliott, M. Schuschnig, K. Grimes, M.S. Dionne, C. Sasakawa, S. Munro, S. Martens, and F. Randow. 2023. TECPR1 conjugates LC3 to damaged endomembranes upon detection of sphingomyelin exposure. *The EMBO Journal*. 42:e113012. doi:10.15252/embj.2022113012.

Cai, S., Y. Wu, A. Guillen-Samander, W. Hancock-Cerutti, J. Liu, and P.D. Camilli. 2022. In situ architecture of the lipid transport protein VPS13C at ER-lysosomes membrane contacts. 2022.03.08.482579. doi:10.1101/2022.03.08.482579.

957 Carter, A.P., A.G. Diamant, and L. Urnavicius. 2016. How dynein and dynactin transport cargos:
958 a structural perspective. *Current Opinion in Structural Biology*. 37:62–70.
959 doi:10.1016/j.sbi.2015.12.003.

960 Chen, W., M.M. Motsinger, J. Li, K.P. Bohannon, and P.I. Hanson. 2024. Ca2+-sensor ALG-2
961 engages ESCRTs to enhance lysosomal membrane resilience to osmotic stress.
962 *Proceedings of the National Academy of Sciences*. 121:e2318412121.
963 doi:10.1073/pnas.2318412121.

964 Clayton, D.F., and J.M. George. 1998. The synucleins: a family of proteins involved in synaptic
965 function, plasticity, neurodegeneration and disease. *Trends in neurosciences*. 21:249–
966 254.

967 Corkery, D.P., S. Castro-Gonzalez, A. Knyazeva, L.K. Herzog, and Y. Wu. 2023. An ATG12-
968 ATG5-TECPR1 E3-like complex regulates unconventional LC3 lipidation at damaged
969 lysosomes. *EMBO reports*. 24:e56841. doi:10.15252/embr.202356841.

970 Corkery, D.P., S. Li, D. Wijayatunga, L.K. Herzog, A. Knyazeva, and Y.-W. Wu. 2024. ESCRT
971 recruitment to damaged lysosomes is dependent on the ATG8 E3-like ligases.
972 2024.04.30.591897. doi:10.1101/2024.04.30.591897.

973 Cross, J., J. Durgan, D.G. McEwan, M. Tayler, K.M. Ryan, and O. Florey. 2023. Lysosome
974 damage triggers direct ATG8 conjugation and ATG2 engagement via non-canonical
975 autophagy. *Journal of Cell Biology*. 222:e202303078. doi:10.1083/jcb.202303078.

976 De Camilli, P., F. Benfenati, F. Valtorta, and P. Greengard. 1990. The Synapsins. *Annual Review*
977 *of Cell and Developmental Biology*. 6:433–460.
978 doi:10.1146/annurev.cb.06.110190.002245.

979 DeGrella, R.F., and R.D. Simoni. 1982. Intracellular transport of cholesterol to the plasma
980 membrane. *Journal of Biological Chemistry*. 257:14256–14262. doi:10.1016/S0021-
981 9258(19)45374-X.

982 Deretic, V., T. Duque, E. Trosdal, M. Paddar, R. Javed, and P. Akepati. 2024. Membrane
983 atg8ylation in Canonical and Noncanonical Autophagy. *Journal of Molecular Biology*.
984 436:168532. doi:10.1016/j.jmb.2024.168532.

985 Durgan, J., and O. Florey. 2022. Many roads lead to CASM: Diverse stimuli of noncanonical
986 autophagy share a unifying molecular mechanism. *Science Advances*. 8:eabo1274.
987 doi:10.1126/sciadv.abo1274.

988 Dziurdzik, S.K., and E. Conibear. 2021. The Vps13 Family of Lipid Transporters and Its Role at
989 Membrane Contact Sites. *International Journal of Molecular Sciences*. 22:2905.
990 doi:10.3390/ijms22062905.

991 Figueras-Novoa, C., L. Timimi, E. Marcassa, R. Ulferts, and R. Beale. 2024. Conjugation of
992 ATG8s to single membranes at a glance. *Journal of Cell Science*. 137:jcs261031.
993 doi:10.1242/jcs.261031.

994 Filippini, F., S. Nola, A. Zahraoui, K. Roger, M. Esmaili, J. Sun, J. Wojnacki, A. Vlieghe, P. Bun,
995 S. Blanchon, J.-C. Rain, J.-M. Taymans, M.-C. Chartier-Harlin, C. Guerrera, and T. Galli.

2023. Secretion of VGF relies on the interplay between LRRK2 and post-Golgi v-SNAREs. *Cell Reports*. 42:112221. doi:10.1016/j.celrep.2023.112221.

Fischer, T.D., C. Wang, B.S. Padman, M. Lazarou, and R.J. Youle. 2020. STING induces LC3B lipidation onto single-membrane vesicles via the V-ATPase and ATG16L1-WD40 domain. *Journal of Cell Biology*. 219:e202009128. doi:10.1083/jcb.202009128.

Fujita, K., S. Kedashiro, T. Yagi, N. Hisamoto, K. Matsumoto, and H. Hanafusa. 2022. The ULK complex–LRRK1 axis regulates Parkin-mediated mitophagy via Rab7 Ser-72 phosphorylation. *Journal of Cell Science*. 135:jcs260395. doi:10.1242/jcs.260395.

Gateva, V., J.K. Sandling, G. Hom, K.E. Taylor, S.A. Chung, X. Sun, W. Ortmann, R. Kosoy, R.C. Ferreira, G. Nordmark, I. Gunnarsson, E. Svenungsson, L. Padyukov, G. Sturfelt, A. Jönsen, A.A. Bengtsson, S. Rantapää-Dahlqvist, E.C. Baechler, E.E. Brown, G.S. Alarcón, J.C. Edberg, R. Ramsey-Goldman, G. McGwin, J.D. Reveille, L.M. Vilá, R.P. Kimberly, S. Manzi, M.A. Petri, A. Lee, P.K. Gregersen, M.F. Seldin, L. Rönnblom, L.A. Criswell, A.-C. Syvänen, T.W. Behrens, and R.R. Graham. 2009. A large-scale replication study identifies TNIP1, PRDM1, JAZF1, UHRF1BP1 and IL10 as risk loci for systemic lupus erythematosus. *Nat Genet*. 41:1228–1233. doi:10.1038/ng.468.

Gillingham, A.K., J. Bertram, F. Begum, and S. Munro. 2019. In vivo identification of GTPase interactors by mitochondrial relocalization and proximity biotinylation. *eLife*. 8:e45916. doi:10.7554/eLife.45916.

Goldman, R., and A. Kaplan. 1973. Rupture of rat liver lysosomes mediated by l-amino acid esters. *Biochimica et Biophysica Acta (BBA) - Biomembranes*. 318:205–216. doi:10.1016/0005-2736(73)90114-4.

Gómez-Sánchez, R., J. Rose, R. Guimarães, M. Mari, D. Papinski, E. Rieter, W.J. Geerts, R. Hardenberg, C. Kraft, C. Ungermann, and F. Reggiori. 2018. Atg9 establishes Atg2-dependent contact sites between the endoplasmic reticulum and phagophores. *The Journal of cell biology*. jcb.201710116. doi:10.1083/jcb.201710116.

Guillén-Samander, A., M. Leonzino, M.G. Hanna IV, N. Tang, H. Shen, and P. De Camilli. 2021. VPS13D bridges the ER to mitochondria and peroxisomes via Miro. *Journal of Cell Biology*. 220. doi:10.1083/jcb.202010004.

Hanna, M., A. Guillén-Samander, and P. De Camilli. 2023. RBG Motif Bridge-Like Lipid Transport Proteins: Structure, Functions, and Open Questions. *Annu. Rev. Cell Dev. Biol.* doi:10.1146/annurev-cellbio-120420-014634.

Hanna, M.G., P.H. Suen, Y. Wu, K.M. Reinisch, and P. De Camilli. 2022. SHIP164 is a chorein motif lipid transfer protein that controls endosome–Golgi membrane traffic. *Journal of Cell Biology*. 221:e202111018. doi:10.1083/jcb.202111018.

Heo, J.-M., A. Ordureau, S. Swarup, J.A. Paulo, K. Shen, D.M. Sabatini, and J.W. Harper. 2018. RAB7A phosphorylation by TBK1 promotes mitophagy via the PINK-PARKIN pathway. *Science Advances*. 4:eaav0443. doi:10.1126/sciadv.aav0443.

Herbst, S., P. Campbell, J. Harvey, E.M. Bernard, V. Papayannopoulos, N.W. Wood, H.R. Morris, and M.G. Gutierrez. 2020. LRRK2 activation controls the repair of damaged

1036 endomembranes in macrophages. *The EMBO Journal*. 39:e104494.
1037 doi:10.15252/embj.2020104494.

1038 Hume, A.N., L.M. Collinson, A. Rapak, A.Q. Gomes, C.R. Hopkins, and M.C. Seabra. 2001.
1039 Rab27a Regulates the Peripheral Distribution of Melanosomes in Melanocytes. *Journal of*
1040 *Cell Biology*. 152:795–808. doi:10.1083/jcb.152.4.795.

1041 John Peter, A.T., B. Herrmann, D. Antunes, D. Rapaport, K.S. Dimmer, and B. Kornmann. 2017.
1042 Vps13-Mcp1 interact at vacuole–mitochondria interfaces and bypass ER–mitochondria
1043 contact sites. *J Cell Biol*. 216:3219–3229. doi:10.1083/jcb.201610055.

1044 John Peter, A.T., S.N.S. van Schie, N.J. Cheung, A.H. Michel, M. Peter, and B. Kornmann. 2022.
1045 Rewiring phospholipid biosynthesis reveals resilience to membrane perturbations and
1046 uncovers regulators of lipid homeostasis. *The EMBO Journal*. 41:e109998.
1047 doi:10.15252/embj.2021109998.

1048 Jumper, J., R. Evans, A. Pritzel, T. Green, M. Figurnov, O. Ronneberger, K. Tunyasuvunakool,
1049 R. Bates, A. Žídek, A. Potapenko, A. Bridgland, C. Meyer, S.A.A. Kohl, A.J. Ballard, A.
1050 Cowie, B. Romera-Paredes, S. Nikolov, R. Jain, J. Adler, T. Back, S. Petersen, D. Reiman,
1051 E. Clancy, M. Zielinski, M. Steinegger, M. Pacholska, T. Berghammer, S. Bodenstein, D.
1052 Silver, O. Vinyals, A.W. Senior, K. Kavukcuoglu, P. Kohli, and D. Hassabis. 2021. Highly
1053 accurate protein structure prediction with AlphaFold. *Nature*. 596:583–589.
1054 doi:10.1038/s41586-021-03819-2.

1055 Kang, Y., K.S. Lehmann, J. Vanegas, H. Long, A. Jefferson, M.A. Freeman, and S. Clark. 2024.
1056 Structural basis of bulk lipid transfer by bridge-like lipid transfer protein LPD-3.
1057 2024.06.21.600134. doi:10.1101/2024.06.21.600134.

1058 Kaur, N., L.R. de la Ballina, H.S. Haukaas, M.L. Torgersen, M. Radulovic, M.J. Munson, A.
1059 Sabirsh, H. Stenmark, A. Simonsen, S.R. Carlsson, and A.H. Lystad. 2023. TECPR1 is
1060 activated by damage-induced sphingomyelin exposure to mediate
1061 noncanonical autophagy. *The EMBO Journal*. 42:e113105.
1062 doi:10.15252/embj.2022113105.

1063 Kumar, N., M. Leonzino, W. Hancock-Cerutti, F.A. Horenkamp, P. Li, J.A. Lees, H. Wheeler, K.M.
1064 Reinisch, and P.D. Camilli. 2018. VPS13A and VPS13C are lipid transport proteins
1065 differentially localized at ER contact sites. *The Journal of cell biology*. 217:3625–3639.
1066 doi:10.1083/jcb.201807019.

1067 Leonzino, M., K.M. Reinisch, and P. De Camilli. 2021. Insights into VPS13 properties and function
1068 reveal a new mechanism of eukaryotic lipid transport. *Biochimica et Biophysica Acta*
1069 *(BBA) - Molecular and Cell Biology of Lipids*. 1866:159003.
1070 doi:10.1016/j.bbalip.2021.159003.

1071 Levine, T.P. 2019. Remote homology searches identify bacterial homologues of eukaryotic lipid
1072 transfer proteins, including Chorein-N domains in TamB and AsmA and Mdm31p. *BMC*
1073 *Molecular and Cell Biology*. 20. doi:10.1186/s12860-019-0226-z.

1074 Levine, T.P. 2022. Sequence Analysis and Structural Predictions of Lipid Transfer Bridges in the
1075 Repeating Beta Groove (RBG) Superfamily Reveal Past and Present Domain Variations

1076 Affecting Form, Function and Interactions of VPS13, ATG2, SHIP164, Hobbit and Tweek.
1077 *Contact*. 5:25152564221134328. doi:10.1177/25152564221134328.

1078 Li, P., J.A. Lees, C.P. Lusk, and K.M. Reinisch. 2020. Cryo-EM reconstruction of a VPS13
1079 fragment reveals a long groove to channel lipids between membranes. *Journal of Cell*
1080 *Biology*. 219. doi:10.1083/jcb.202001161.

1081 Lin, S.X., W.G. Mallet, A.Y. Huang, and F.R. Maxfield. 2003. Endocytosed Cation-Independent
1082 Mannose 6-Phosphate Receptor Traffics via the Endocytic Recycling Compartment en
1083 Route to the trans-Golgi Network and a Subpopulation of Late Endosomes. *MBoC*.
1084 15:721–733. doi:10.1091/mbc.e03-07-0497.

1085 Maeda, S., C. Otomo, and T. Otomo. 2019. The autophagic membrane tether ATG2A transfers
1086 lipids between membranes. *eLife*. 8:e45777. doi:10.7554/eLife.45777.

1087 Mallard, F., B.L. Tang, T. Galli, D. Tenza, A. Saint-Pol, X. Yue, C. Antony, W. Hong, B. Goud, and
1088 L. Johannes. 2002. Early/recycling endosomes-to-TGN transport involves two SNARE
1089 complexes and a Rab6 isoform. *The Journal of cell biology*. 156:653–664.
1090 doi:10.1083/jcb.200110081.

1091 Martinez-Arca, S., S. Coco, G. Mainguy, U. Schenk, P. Alberts, P. Bouillé, M. Mezzina, A.
1092 Prochiantz, M. Matteoli, D. Louvard, and T. Galli. 2001. A Common Exocytotic Mechanism
1093 Mediates Axonal and Dendritic Outgrowth. *J. Neurosci.* 21:3830–3838.
1094 doi:10.1523/JNEUROSCI.21-11-03830.2001.

1095 Melia, T.J., A.H. Lystad, and A. Simonsen. 2020. Autophagosome biogenesis: From membrane
1096 growth to closure. *Journal of Cell Biology*. 219:e202002085. doi:10.1083/jcb.202002085.

1097 Ménasché, G., E. Pastural, J. Feldmann, S. Certain, F. Ersoy, S. Dupuis, N. Wulffraat, D. Bianchi,
1098 A. Fischer, F. Le Deist, and G. de Saint Basile. 2000. Mutations in RAB27A cause Griscelli
1099 syndrome associated with haemophagocytic syndrome. *Nat Genet*. 25:173–176.
1100 doi:10.1038/76024.

1101 Meyer, H., and B. Kravic. 2024. The Endo-Lysosomal Damage Response. *Annual Review of*
1102 *Biochemistry*. 93:367–387. doi:10.1146/annurev-biochem-030222-102505.

1103 Milovanovic, D., and P. De Camilli. 2017. Synaptic Vesicle Clusters at Synapses: A Distinct Liquid
1104 Phase? *Neuron*. 93:995–1002. doi:10.1016/j.neuron.2017.02.013.

1105 Milovanovic, D., Y. Wu, X. Bian, and P. De Camilli. 2018. A liquid phase of synapsin and lipid
1106 vesicles. *Science*. 361:604–607. doi:10.1126/science.aat5671.

1107 Nagashima, K., S. Torii, Z. Yi, M. Igarashi, K. Okamoto, T. Takeuchi, and T. Izumi. 2002.
1108 Melanophilin directly links Rab27a and myosin Va through its distinct coiled-coil regions.
1109 *FEBS Letters*. 517:233–238. doi:10.1016/S0014-5793(02)02634-0.

1110 Nagata, K., T. Satoh, H. Itoh, T. Kozasa, Y. Okano, T. Doi, Y. Kaziro, and Y. Nozawa. 1990. The
1111 ram: A novel low molecular weight GTP-binding protein cDNA from a rat megakaryocyte
1112 library. *FEBS Letters*. 275:29–32. doi:10.1016/0014-5793(90)81431-M.

1113 Neuman, S.D., T.P. Levine, and A. Bashirullah. 2022. A novel superfamily of bridge-like lipid
1114 transfer proteins. *Trends in Cell Biology*. 32:962–974. doi:10.1016/j.tcb.2022.03.011.

1115 Nieto-Torres, J.L., A.M. Leidal, J. Debnath, and M. Hansen. 2021. Beyond Autophagy: The
1116 Expanding Roles of ATG8 Proteins. *Trends in Biochemical Sciences*. 46:673–686.
1117 doi:10.1016/j.tibs.2021.01.004.

1118 Nirujogi, R.S., F. Tonelli, M. Taylor, P. Lis, A. Zimprich, E. Sammler, and D.R. Alessi. 2021.
1119 Development of a multiplexed targeted mass spectrometry assay for LRRK2-
1120 phosphorylated Rabs and Ser910/Ser935 biomarker sites. *Biochemical Journal*. 478:299–
1121 326. doi:10.1042/BCJ20200930.

1122 Osawa, T., T. Kotani, T. Kawaoka, E. Hirata, K. Suzuki, H. Nakatogawa, Y. Ohsumi, and N.N.
1123 Noda. 2019. Atg2 mediates direct lipid transfer between membranes for autophagosome
1124 formation. *Nat Struct Mol Biol*. 26:281–288. doi:10.1038/s41594-019-0203-4.

1125 Otto, G.P., M. Razi, J. Morvan, F. Stenner, and S.A. Tooze. 2010. A novel syntaxin 6-interacting
1126 protein, SHIP164, regulates syntaxin 6-dependent sorting from early endosomes. *Traffic*
1127 *(Copenhagen, Denmark)*. 11:688–705. doi:10.1111/j.1600-0854.2010.01049.x.

1128 Palade, G. 1975. Intracellular Aspects of the Process of Protein Synthesis. *Science*. 189:347–
1129 358. doi:10.1126/science.1096303.

1130 Park, D., Y. Wu, S.-E. Lee, G. Kim, S. Jeong, D. Milovanovic, P. De Camilli, and S. Chang. 2021.
1131 Cooperative function of synaptophysin and synapsin in the generation of synaptic vesicle-
1132 like clusters in non-neuronal cells. *Nat Commun*. 12:263. doi:10.1038/s41467-020-20462-
1133 z.

1134 Park, J.-S., and A.M. Neiman. 2012. VPS13 regulates membrane morphogenesis during
1135 sporulation in Saccharomyces cerevisiae. *Journal of Cell Science*. 125:3004–3011.
1136 doi:10.1242/jcs.105114.

1137 Park, J.-S., M.K. Thorsness, R. Policastro, L.L. McGoldrick, N.M. Hollingsworth, P.E. Thorsness,
1138 and A.M. Neiman. 2016. Yeast Vps13 promotes mitochondrial function and is localized at
1139 membrane contact sites. *MBoC*. 27:2435–2449. doi:10.1091/mbc.E16-02-0112.

1140 Pols, M.S., E. van Meel, V. Oorschot, C. ten Brink, M. Fukuda, M.G. Swetha, S. Mayor, and J.
1141 Klumperman. 2013. hVps41 and VAMP7 function in direct TGN to late endosome
1142 transport of lysosomal membrane proteins. *Nat Commun*. 4:1361.
1143 doi:10.1038/ncomms2360.

1144 Prinz, W.A., A. Toulmay, and T. Balla. 2020. The functional universe of membrane contact sites.
1145 *Nature Reviews Molecular Cell Biology*. 21:7–24. doi:10.1038/s41580-019-0180-9.

1146 Radulovic, M., K.O. Schink, E.M. Wenzel, V. Nähse, A. Bongiovanni, F. Lafont, and H. Stenmark.
1147 2018. ESCRT-mediated lysosome repair precedes lysophagy and promotes cell survival.
1148 *The EMBO Journal*. 37:e99753. doi:10.15252/embj.201899753.

1149 Radulovic, M., E.M. Wenzel, S. Gilani, L.K. Holland, A.H. Lystad, S. Phuyal, V.M. Olkkonen, A.
1150 Brech, M. Jäättelä, K. Maeda, C. Raiborg, and H. Stenmark. 2022. Cholesterol transfer

via endoplasmic reticulum contacts mediates lysosome damage repair. *The EMBO Journal*. 41:e112677. doi:10.15252/embj.2022112677.

Reinisch, K.M., and W.A. Prinz. 2021. Mechanisms of nonvesicular lipid transport. *Journal of Cell Biology*. 220. doi:10.1083/jcb.202012058.

Saheki, Y., and P.D. Camilli. 2017. Endoplasmic Reticulum-Plasma Membrane Contact Sites. *Annual review of biochemistry*. 86:659–684. doi:10.1146/annurev-biochem-061516-044932.

Shukla, S., K.P. Larsen, C. Ou, K. Rose, and J.H. Hurley. 2022. In vitro reconstitution of calcium-dependent recruitment of the human ESCRT machinery in lysosomal membrane repair. *Proceedings of the National Academy of Sciences*. 119:e2205590119. doi:10.1073/pnas.2205590119.

Skowyra, M.L., P.H. Schlesinger, T.V. Naismith, and P.I. Hanson. 2018. Triggered recruitment of ESCRT machinery promotes endolysosomal repair. *Science*. 360:eaar5078. doi:10.1126/science.aar5078.

Stenmark, H., and V.M. Olkkonen. 2001. The Rab GTPase family. *Genome Biology*. 2:reviews3007.1. doi:10.1186/gb-2001-2-5-reviews3007.

Strom, M., A.N. Hume, A.K. Tarafder, E. Barkagianni, and M.C. Seabra. 2002. A Family of Rab27-binding Proteins: MELANOPHILIN LINKS Rab27a AND MYOSIN Va FUNCTION IN MELANOSOME TRANSPORT*. *Journal of Biological Chemistry*. 277:25423–25430. doi:10.1074/jbc.M202574200.

Südhof, T.C., A.J. Czernik, H.-T. Kao, K. Takei, P.A. Johnston, A. Horiuchi, S.D. Kanazir, M.A. Wagner, M.S. Perin, P. De Camilli, and P. Greengard. 1989. Synapsins: Mosaics of Shared and Individual Domains in a Family of Synaptic Vesicle Phosphoproteins. *Science*. 245:1474–1480. doi:10.1126/science.2506642.

Talaia, G., A. Bentley-DeSousa, and S.M. Ferguson. 2024. Lysosomal TBK1 responds to amino acid availability to relieve Rab7-dependent mTORC1 inhibition. *The EMBO Journal*. 1–20. doi:10.1038/s44318-024-00180-8.

Tan, J.X., and T. Finkel. 2022. A phosphoinositide signalling pathway mediates rapid lysosomal repair. *Nature*. 1–7. doi:10.1038/s41586-022-05164-4.

Thiele, D.L., and P.E. Lipsky. 1990. Mechanism of L-leucyl-L-leucine methyl ester-mediated killing of cytotoxic lymphocytes: dependence on a lysosomal thiol protease, dipeptidyl peptidase I, that is enriched in these cells. *Proceedings of the National Academy of Sciences*. 87:83–87. doi:10.1073/pnas.87.1.83.

Tokai, M., H. Kawasaki, Y. Kikuchi, and K. Ouchi. 2000. Cloning and Characterization of the CSF1 Gene ofSaccharomyces cerevisiae, Which Is Required for Nutrient Uptake at Low Temperature. *Journal of Bacteriology*. 182:2865–2868. doi:10.1128/JB.182.10.2865-2868.2000.

1188 Tran, T.H.T., Q. Zeng, and W. Hong. 2007. VAMP4 cycles from the cell surface to the trans-Golgi
1189 network via sorting and recycling endosomes. *Journal of Cell Science*. 120:1028–1041.
1190 doi:10.1242/jcs.03387.

1191 Tu, Y.X., and J. Brumell. 2020. Examining the Autophagy Proximity Interactome. University of
1192 Toronto.

1193 Uchimoto, T., H. Nohara, R. Kamehara, M. Iwamura, N. Watanabe, and Y. Kobayashi. 1999.
1194 Mechanism of apoptosis induced by a lysosomotropic agent, L-Leucyl-L-Leucine methyl
1195 ester. *Apoptosis*. 4:357–362. doi:https://doi.org/10.1023/A:1009695221038.

1196 Unoki, M., T. Nishidate, and Y. Nakamura. 2004. ICBP90, an E2F-1 target, recruits HDAC1 and
1197 binds to methyl-CpG through its SRA domain. *Oncogene*. 23:7601–7610.
1198 doi:10.1038/sj.onc.1208053.

1199 Valverde, D.P., S. Yu, V. Boggavarapu, N. Kumar, J.A. Lees, T. Walz, K.M. Reinisch, and T.J.
1200 Melia. 2019. ATG2 transports lipids to promote autophagosome biogenesis.
1201 *Journal of Cell Biology*. 218:1787–1798. doi:10.1083/jcb.201811139.

1202 Velikkakath, A.K.G., T. Nishimura, E. Oita, N. Ishihara, and N. Mizushima. 2012. Mammalian Atg2
1203 proteins are essential for autophagosome formation and important for regulation of size
1204 and distribution of lipid droplets. *MBoC*. 23:896–909. doi:10.1091/mbc.e11-09-0785.

1205 Voeltz, G.K., E.M. Sawyer, G. Hajnóczky, and W.A. Prinz. 2024. Making the connection: How
1206 membrane contact sites have changed our view of organelle biology. *Cell*. 187:257–270.
1207 doi:10.1016/j.cell.2023.11.040.

1208 Wang, C., B. Wang, T. Pandey, Y. Long, J. Zhang, F. Oh, J. Sima, R. Guo, Y. Liu, C. Zhang, S.
1209 Mukherjee, M. Bassik, W. Lin, H. Deng, G. Vale, J.G. McDonald, K. Shen, and D.K. Ma.
1210 2022. A conserved megaprotein-based molecular bridge critical for lipid trafficking and
1211 cold resilience. *Nat Commun*. 13:6805. doi:10.1038/s41467-022-34450-y.

1212 Wang, C.-W., J. Kim, W.-P. Huang, H. Abeliovich, P.E. Stromhaug, W.A. Dunn, and D.J. Klionsky.
1213 2001. Apg2 Is a Novel Protein Required for the Cytoplasm to Vacuole Targeting,
1214 Autophagy, and Pexophagy Pathways *. *Journal of Biological Chemistry*. 276:30442–
1215 30451. doi:10.1074/jbc.M102342200.

1216 Wang, G., S. Nola, S. Bovio, P. Bun, M. Coppey-Moisan, F. Lafont, and T. Galli. 2018.
1217 Biomechanical Control of Lysosomal Secretion Via the VAMP7 Hub: A Tug-of-War
1218 between VARP and LRRK1. *iScience*. 4:127–143. doi:10.1016/j.isci.2018.05.016.

1219 Wang, X., P. Xu, A. Bentley-DeSousa, W. Hancock-Cerutti, S. Cai, B.T. Johnson, F. Tonelli, G.
1220 Talaia, D.R. Alessi, S.M. Ferguson, and P.D. Camilli. 2024a. Lysosome damage triggers
1221 acute formation of ER to lysosomes membrane tethers mediated by the bridge-like lipid
1222 transport protein VPS13C. 2024.06.08.598070. doi:10.1101/2024.06.08.598070.

1223 Wang, Y., S. Dahmane, R. Ti, X. Mai, L. Zhu, L.-A. Carlson, and G. Stjepanovic. 2024b. Structural
1224 basis for lipid transfer by the ATG2A–ATG9A complex. *Nat Struct Mol Biol*. 1–13.
1225 doi:10.1038/s41594-024-01376-6.

1226 Wang, Y., W. Huynh, T.D. Skokan, W. Lu, A. Weiss, and R.D. Vale. 2019. CRACR2a is a calcium-
1227 activated dynein adaptor protein that regulates endocytic traffic. *Journal of Cell Biology*.
1228 218:1619–1633. doi:10.1083/jcb.201806097.

1229 Wen, L., L. Liu, X. Shen, H. Li, Z. Zhu, H. Huang, M. Cai, D. Qian, S. Shen, Y. Qiu, Y. Cui, and Y.
1230 Sheng. 2020. The association of the UHRF1BP1 gene with systemic lupus erythematosus
1231 was replicated in a Han Chinese population from mainland China. *Annals of Human*
1232 *Genetics*. 84:221–228. doi:10.1111/ahg.12362.

1233 Wirtz, K.W.A. 1991. Phospholipid transfer proteins: From lipid monolayers to cells. *Klin*
1234 *Wochenschr*. 69:105–111. doi:10.1007/BF01795953.

1235 Wong, L.H., A.T. Gatta, and T.P. Levine. 2019. Lipid transfer proteins: the lipid commute via
1236 shuttles, bridges and tubes. *Nat Rev Mol Cell Biol*. 20:85–101. doi:10.1038/s41580-018-
1237 0071-5.

1238 Yang, J., I. Anishchenko, H. Park, Z. Peng, S. Ovchinnikov, and D. Baker. 2020. Improved protein
1239 structure prediction using predicted interresidue orientations. *PNAS*. 117:1496–1503.
1240 doi:10.1073/pnas.1914677117.

1241 Yariv, B., E. Yariv, A. Kessel, G. Masrati, A.B. Chorin, E. Martz, I. Mayrose, T. Pupko, and N.
1242 Ben-Tal. 2023. Using evolutionary data to make sense of macromolecules with a "face-
1243 lifted" ConSurf. *Protein Science*. 32:e4582. doi:10.1002/pro.4582.

1244 Zhang, Y., W. Yang, C.C. Mok, T.M. Chan, R.W.S. Wong, M.Y. Mok, K.W. Lee, S.N. Wong,
1245 A.M.H. Leung, T.L. Lee, M.H.K. Ho, P.P.W. Lee, W.H.S. Wong, J. Yang, J. Zhang, C.-M.
1246 Wong, I.O.L. Ng, M.-M. Garcia-Barceló, S.S. Cherny, P.K.-H. Tam, P.C. Sham, C.S. Lau,
1247 and Y.L. Lau. 2011. Two missense variants in UHRF1BP1 are independently associated
1248 with systemic lupus erythematosus in Hong Kong Chinese. *Genes Immun*. 12:231–234.
1249 doi:10.1038/gene.2010.66.

1250

Figure 1

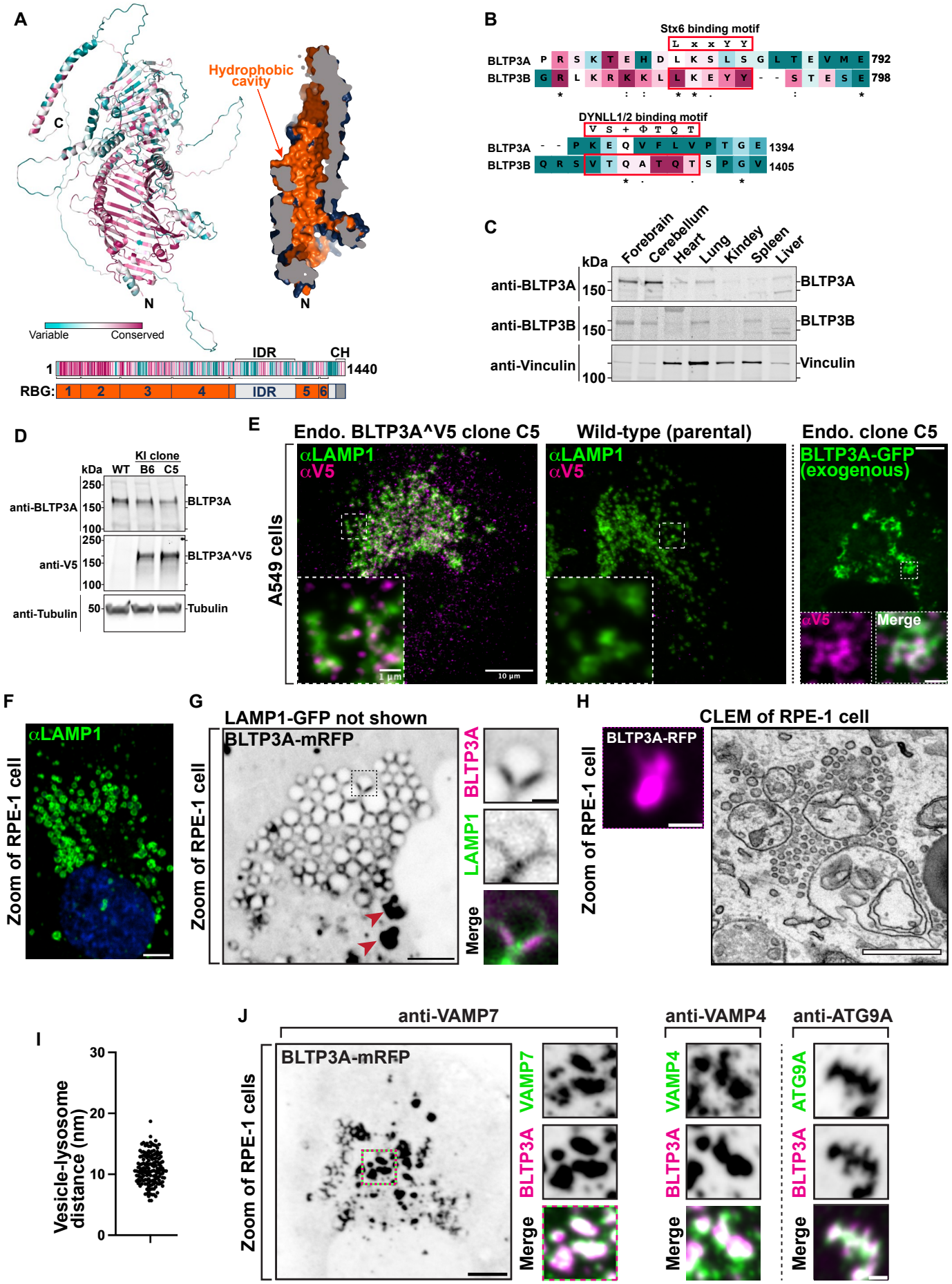
A
Hydrophobic cavity
C
N
N
Variable
Conserved
IDR
CH
1
1440
RBG:
1
2
3
4
IDR
5
6
B
Stx6 binding motif
L x x Y Y
BLTP3A P R S K T E H D L K S L S G L T E V M E 792
BLTP3B G R L K R K K L L K E Y Y - - S T E S E 798
DYNLL1/2 binding motif
V S + Φ T Q T
BLTP3A - - P K E Q V F L V P T G E 1394
BLTP3B Q R S V T Q A T Q T S P G V 1405
C
Forebrain
Cerebellum
Heart
Lung
Kindey
Spleen
Liver
kDa
anti-BLTP3A
150
BLTP3A
anti-BLTP3B
150
BLTP3B
anti-Vinculin
100
Vinculin
D
KI clone
kDa
WT
B6
C5
250
150
100
anti-BLTP3A
BLTP3A
250
150
100
anti-V5
BLTP3A^V5
anti-Tubulin
50
Tubulin
E
Endo. BLTP3A^V5 clone C5
Wild-type (parental)
Endo. clone C5
A549 cells
αLAMP1
αV5
αLAMP1
αV5
BLTP3A-GFP
(exogenous)
αV5
Merge
1 µm
10 µm
F
Zoom of RPE-1 cell
αLAMP1
G
LAMP1-GFP not shown
Zoom of RPE-1 cell
BLTP3A-mRFP
BLTP3A
LAMP1
Merge
H
CLEM of RPE-1 cell
Zoom of RPE-1 cell
BLTP3A-RFP
I
Vesicle-lysosome distance (nm)
30
20
10
0
J
anti-VAMP7
anti-VAMP4
anti-ATG9A
Zoom of RPE-1 cells
BLTP3A-mRFP
VAMP7
BLTP3A
Merge
VAMP4
BLTP3A
Merge
ATG9A
BLTP3A
Merge

Figure 2

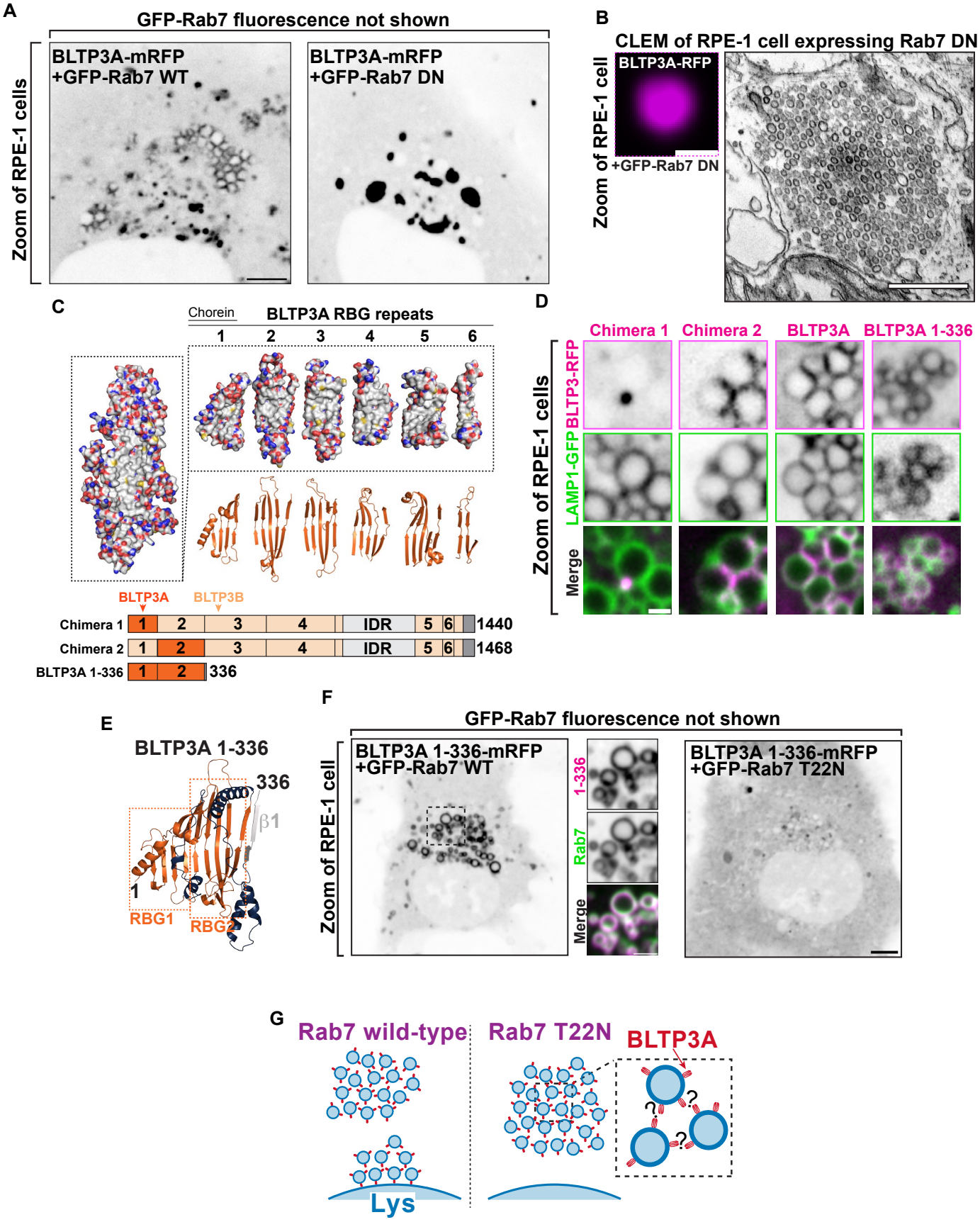
A
GFP-Rab7 fluorescence not shown
Zoom of RPE-1 cells
BLTP3A-mRFP
+GFP-Rab7 WT
BLTP3A-mRFP
+GFP-Rab7 DN
B
CLEM of RPE-1 cell expressing Rab7 DN
Zoom of RPE-1 cell
BLTP3A-RFP
+GFP-Rab7 DN
C
Chorein
BLTP3A RBG repeats
1 2 3 4 5 6
BLTP3A
BLTP3B
Chimera 1 1 2 3 4 IDR 5 6 1440
Chimera 2 1 2 3 4 IDR 5 6 1468
BLTP3A 1-336 1 2 336
D
Chimera 1
Chimera 2
BLTP3A
BLTP3A 1-336
Zoom of RPE-1 cells
BLTP3-RFP
LAMP1-GFP
Merge
E
BLTP3A 1-336
336
β1
1
RBG1
RBG2
F
GFP-Rab7 fluorescence not shown
Zoom of RPE-1 cell
BLTP3A 1-336-mRFP
+GFP-Rab7 WT
1-336
Rab7
Merge
BLTP3A 1-336-mRFP
+GFP-Rab7 T22N
G
Rab7 wild-type
Rab7 T22N
BLTP3A
Lys

Figure 3

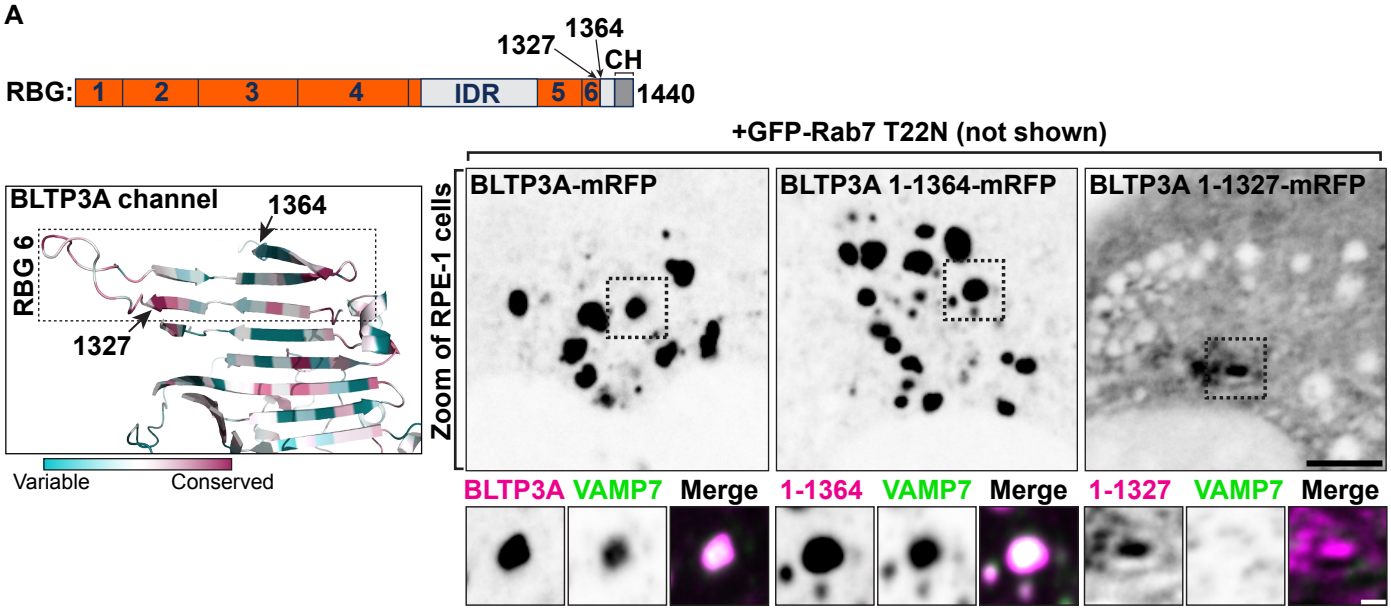
A
1327
1364
CH
RBG:
1
2
3
4
IDR
5
6
1440
+GFP-Rab7 T22N (not shown)
BLTP3A channel
1364
RBG 6
1327
Variable
Conserved
Zoom of RPE-1 cells
BLTP3A-mRFP
BLTP3A 1-1364-mRFP
BLTP3A 1-1327-mRFP
BLTP3A VAMP7 Merge
1-1364 VAMP7 Merge
1-1327 VAMP7 Merge

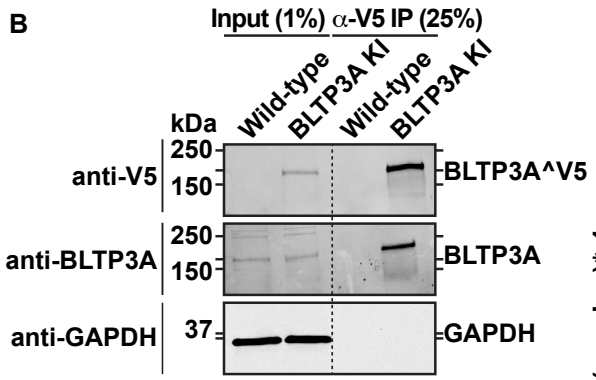
B
Input (1%)
α-V5 IP (25%)
Wild-type
BLTP3A KI
Wild-type
BLTP3A KI
kDa
anti-V5
250
150
BLTP3A^V5
anti-BLTP3A
250
150
BLTP3A
anti-GAPDH
37
GAPDH

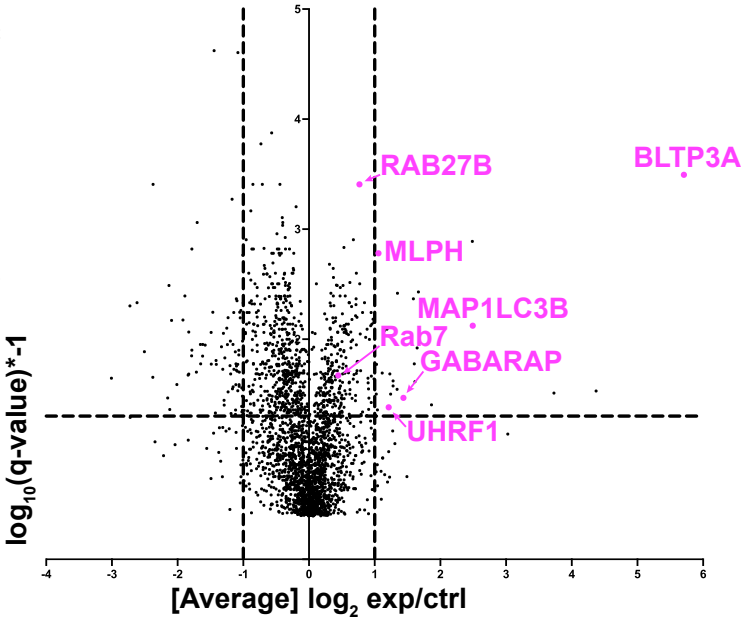
C
RAB27B
BLTP3A
MLPH
MAP1LC3B
Rab7
GABARAP
UHRF1
log10(q-value)*-1
[Average] log2 exp/ctrl

Figure 4

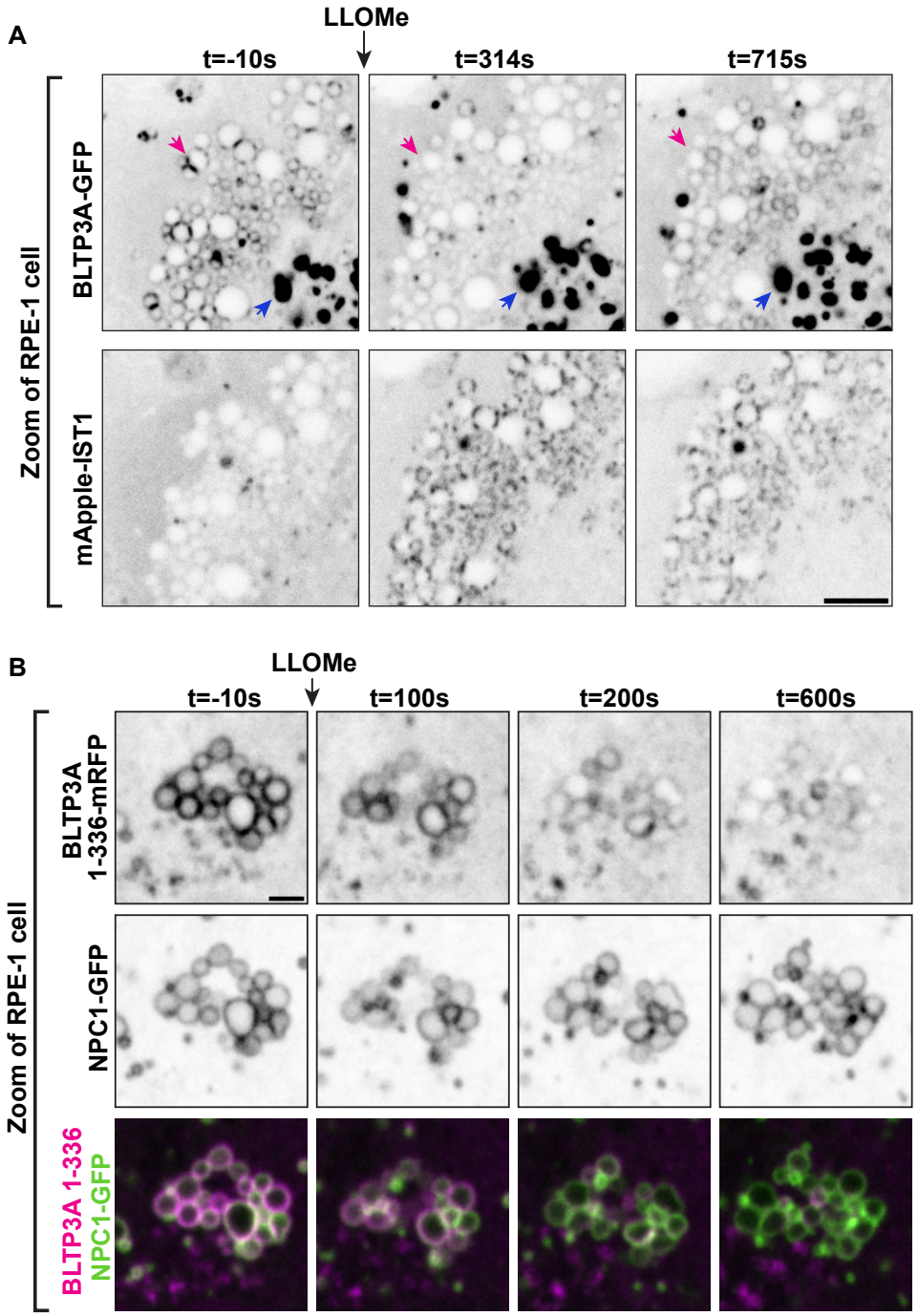
A
LLOMe
t=-10s
t=314s
t=715s
Zoom of RPE-1 cell
BLTP3A-GFP
mApple-IST1
B
LLOMe
t=-10s
t=100s
t=200s
t=600s
Zoom of RPE-1 cell
BLTP3A 1-336-mRFP
NPC1-GFP
BLTP3A 1-336
NPC1-GFP

Figure 5

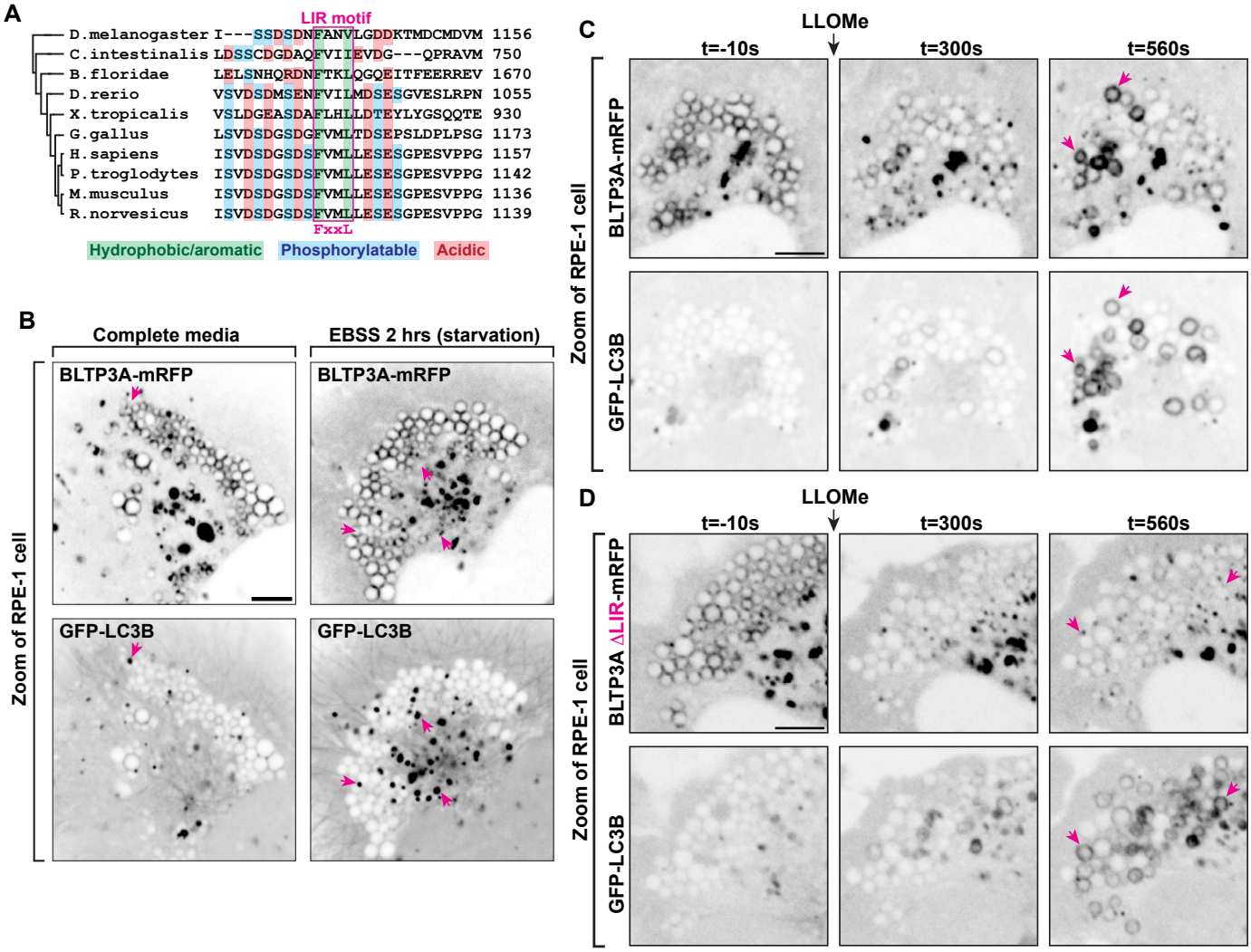
A
LIR motif
D.melanogaster I---SSDSDNFANVLGDDKTMDCMDVM 1156
C.intestinalis LDSSCDGDAQFVIIEVDG---QPRAVM 750
B.floridae LELSNHQRDNFTKLQGQEITFEERREV 1670
D.rerio VSVDSDMSENFVILMDSESGVESLRPN 1055
X.tropicalis VSLDGEASDAFLHLLDTEYLYGSQQTE 930
G.gallus LSVDSDGSDGFVMLTDSEPSLDPLPSG 1173
H.sapiens ISVDSDGSDSFVMLLESESGPESVPPG 1157
P.troglodytes ISVDSDGSDSFVMLLESESGPESVPPG 1142
M.musculus ISVDSDGSDSFVMLLESESGPESVPPG 1136
R.norvesicus ISVDSDGSDSFVMLLESESGPESVPPG 1139
FxxL
Hydrophobic/aromatic
Phosphorylatable
Acidic
B
Complete media
EBSS 2 hrs (starvation)
BLTP3A-mRFP
GFP-LC3B
Zoom of RPE-1 cell
C
LLOMe
t=-10s
t=300s
t=560s
BLTP3A-mRFP
GFP-LC3B
Zoom of RPE-1 cell
D
LLOMe
t=-10s
t=300s
t=560s
BLTP3A ΔLIR-mRFP
GFP-LC3B
Zoom of RPE-1 cell

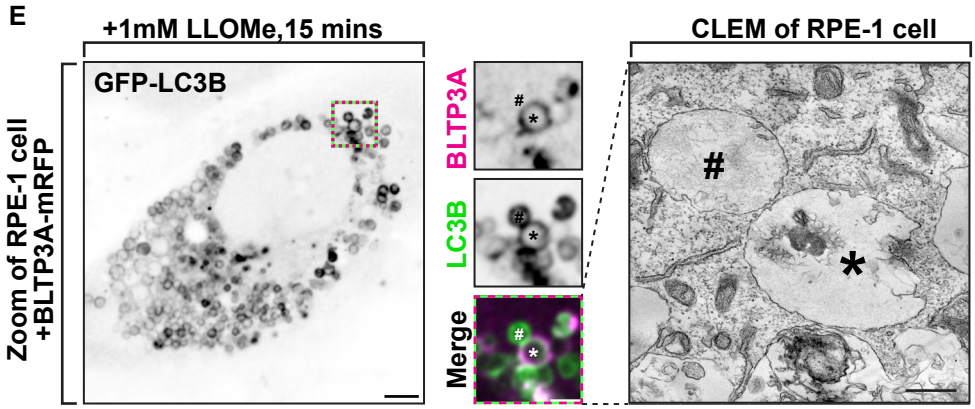
E
+1mM LLOMe,15 mins
GFP-LC3B
Zoom of RPE-1 cell
+BLTP3A-mRFP
BLTP3A
LC3B
Merge
CLEM of RPE-1 cell
#
*

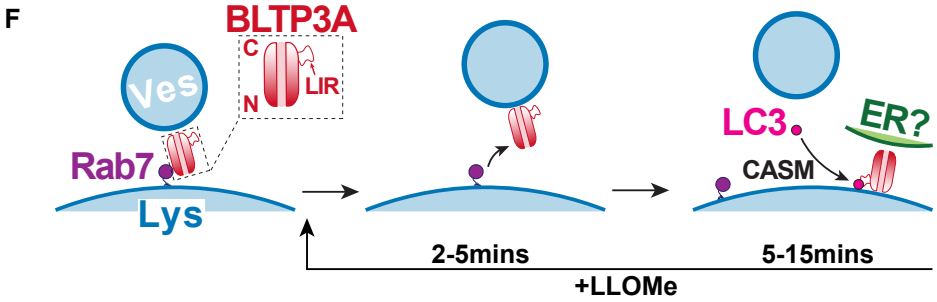
F
BLTP3A
C
N
LIR
Ves
Rab7
Lys
LC3
ER?
CASM
2-5mins
5-15mins
+LLOMe

Supplemental Figure 1

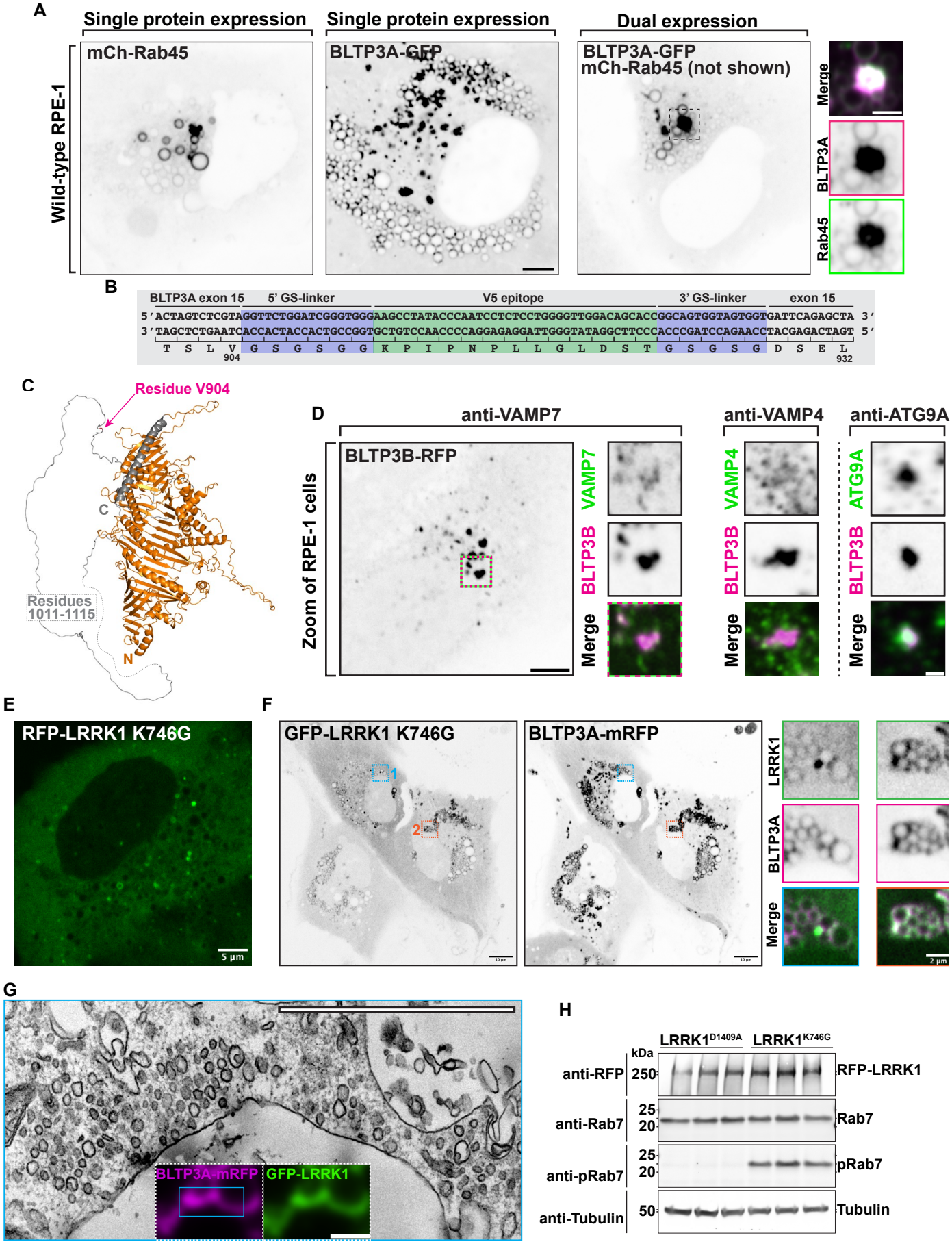

Supplemental Figure 2

A

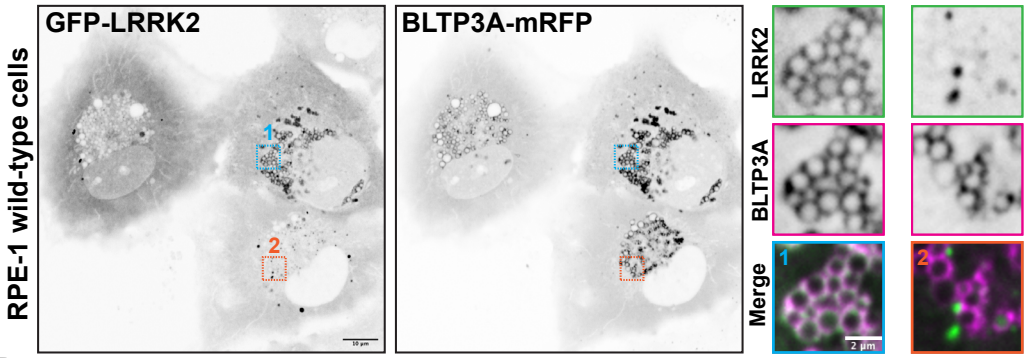

B

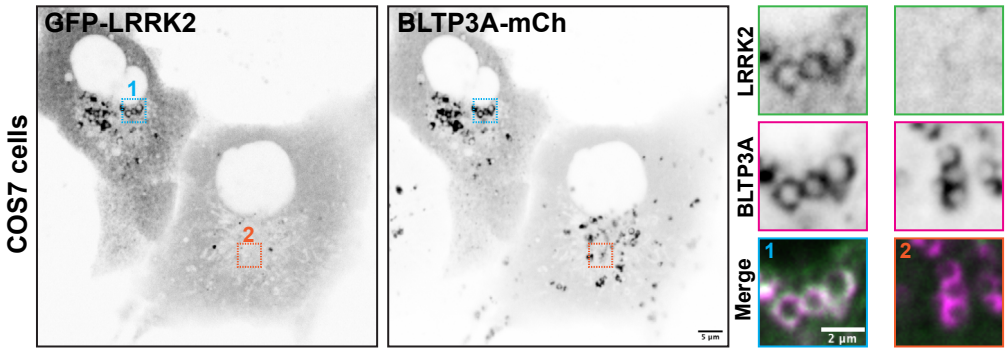

C

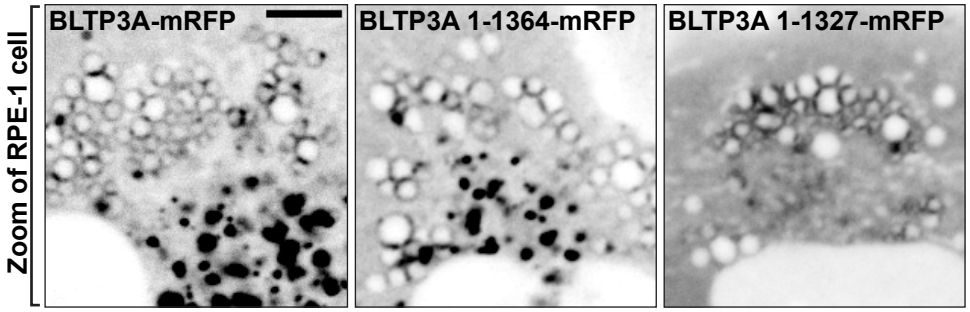

D

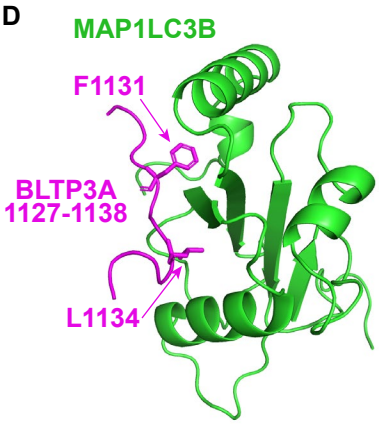

E

AF3 predictions of BLTP3A with mAtg8 proteins

BLTP3A:	1110-1150		1110-1150 ΔLIR	
	ipTM	pTM	ipTM	pTM
MAP1LC3A	0.66	0.7	0.31	0.69
MAP1LC3B	0.56	0.68	0.32	0.7
MAP1LC3C	0.57	0.62	0.32	0.62
GABARAP	0.74	0.76	0.55	0.74
GABARAPL1	0.73	0.75	0.52	0.72
GABARAPL2	0.72	0.74	0.53	0.73
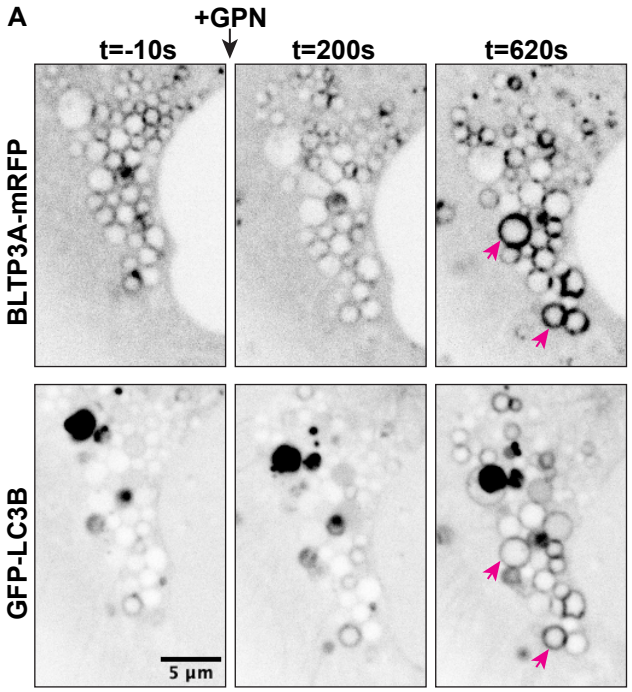
Supplemental Figure 3